

Forecasting Gamma-Ray Bursts using Gravitational Waves

Sarp Akcay¹

¹*School of Mathematics & Statistics, University College Dublin, Belfield, Dublin 4, Ireland.*

(Dated: April 3, 2018)

We explore the intriguing possibility of employing future ground-based gravitational-wave interferometers to detect the inspiral of binary neutron stars early enough to alert electromagnetic observatories so that a gamma-ray burst (GRB) can be observed in its entirety from its very start. We quantify the ability to predict a GRB by computing the time a binary neutron star (BNS) system takes to inspiral from its moment of detection to its final merger. We define the moment of detection to be the instant at which the inteferometer network accumulates a signal-to-noise ratio of 15. For our computations, we specifically consider BNS systems at luminosity distances of (i) $D \leq 200$ Mpc in the three-interferometer Advanced-LIGO-Virgo network of 2020, and (ii) $D \leq 1000$ Mpc in the Einstein Telescope’s B and C configurations. In the case of Advanced LIGO-Virgo we find that we may at best get a few minutes of warning time thus we expect no forecast of GRBs in the 2020s. On the other hand, Einstein Telescope will provide us with advance warning times up to five hours. Taking one hour as a benchmark warning time, we obtain a corresponding horizon distance of roughly 600 Mpc for the Einstein Telescope C configuration. Using current BNS event rates within this horizon distance, we show that this translates to forecasts of $\gtrsim \mathcal{O}(10^2)$ GRBs in the 2030s. We reapply our warning-time computation to binary black hole - neutron star inspirals and find that we expect 1 to 3 tidal disruption events to be forecast by the same detector.

I. Introduction

The 6.95¹ gravitational-wave merger events detected by the Advanced Ligo-Virgo network have firmly established gravitational-wave astronomy as an observational science [1–5]. Though the first event of 14 September 2015 (GW150914 [6]) will always be the “poster-child” of this field, the icing on the cake was the 17 August 2017 (GW170817 [5]) event involving the inspiral and merger of a binary neutron star system promptly followed, 1.7 seconds later, by a gamma-ray burst (GRB170817A) detected by the Fermi Gamma-ray Burst Monitor [7] and by the International Gamma-Ray Astrophysics Laboratory [8, 9]. The Advanced-LIGO-Virgo network’s initial source localization to within 31 degree² in the Southern skies enabled astronomers to locate the electromagnetic counterpart in the galaxy NGC 4993, first picked up by the One-Meter, Two Hemisphere team less than 11 hours after the merger [10, 11]. This subsequently launched the largest-ever campaign of multi-messenger astronomy across the entire electromagnetic (EM) spectrum which is still ongoing more than half a year after the initial GRB [12].

GW170817 was initially identified by the LIGO-Hanford interferometer (H1) using a template bank of gravitational waveforms computed within the framework of post-Newtonian theory [13, 14]. The inspiral swept across the Advanced Ligo-Virgo (ALV) network’s bandwidth from approximately 30 Hz to about 2 kHz in 57 seconds executing nearly 3000 gravitational wave cycles and accumulating a network signal-to-noise ratio of 32.4 with a false-alarm rate of one per 8.0×10^4 years [5]. The total mass of the system was inferred to be $2.74^{+0.04}_{-0.01} M_{\odot}$ with component masses in the range $1.17 - 1.60 M_{\odot}$ consistent with neutron stars (assuming low spin priors, see Sec. IV). Moreover, both the gravitational wave (GW) and EM observations were consistent with a source luminosity distance of ~ 40 Mpc and supported the hypothesis that GW170817 resulted from the inspiral and merger of two neutron stars, causing the prompt short-hard gamma-ray burst (GRB170817A) in NGC4993 as first suggested by Ref. [15].

A week after GW170817, the ALV network was taken offline for upgrades for the third observation run (O3) scheduled to start in Autumn 2018 with roughly twice the sensitivity of O2. In addition, the Japanese cryogenic interferometer KAGRA ([16, 17]) will start its test runs in 2018-2019 and reach its design sensitivity circa 2021-2022 [18, 19]. By 2025, LIGO-India detector will join the global interferometer network hence improving both the overall sensitivity and the sky-localization capabilities [19]. Around this time, the construction of the first third-generation ground-based interferometer, Einstein Telescope, will begin in Europe [20]. Meanwhile, the US is currently considering a mid-2020s update to LIGO called Voyager [21] and the construction

¹ There have thus far been six detections with 5σ statistical significance and one additional event, LVT151012 [1], with $2\sigma \simeq 95\%$ significance hence 6.95 overall.

of a more ambitious 40 km long interferometer dubbed The Cosmic Explorer [22]. All of these near-future additions to the GW-detector network beg a simple question: can we detect the inspiral of a binary neutron star system early enough to witness a gamma-ray burst as it happens? In other words, can we forecast GRBs using GW detections?

The short answer is in the affirmative. The long answer is still affirmative, but depends on many factors such as source distance and sky position, detector sensitivity and orientation. One also needs to account for the fact that GRBs are thought to be collimated emissions with narrow outburst angles [23]. As such, most GRBs that occur in the universe are electromagnetically undetectable. Fortunately, this was not the case with GRB170817A, but even for a reasonable GRB jet opening angle of $\sim 10^\circ$, we expect to observe $\sim 10\%$ of neutron star mergers as GRBs [24]. However, it is possible that some of the near-Earth pointing short hard GRBs may be observed as long-duration GRBs or X-ray flashes thus increasing this percentage [25].

Given the sensitivities of interferometers to date, efforts have thus far mostly focused on reducing the latency of EM follow-ups, i.e., the lag time between the merger and the alerting of the EM observatories. LIGO-Virgo science runs in 2009-2010 yielded a latency of ~ 30 to 60 minutes [26] (no detections). In the case of GW170817, the latency was 40 minutes and $36^{+1.7}$ seconds [12]. It then took an additional 10 hours to locate the optical transient.

Here, we are interested in exploring the predictive power of near-future ground-based GW detectors. More specifically, we wish to find out how much early warning the GW detectors can provide us before the merger/GRB. Ref. [27] approached this from an algorithmic perspective by developing computationally inexpensive methods to detect inspiral signals in GW data to provide early-warning triggers *before* the merger (also see Ref. [28] for a very recent improvement to what is currently being used in the ALV pipeline). We instead focus on the forecasting capabilities of the ground-based interferometers at their *full design* sensitivity by computing the time interval between the merger and the instant of detection defined in terms of a certain threshold signal-to-noise ratio. To this end, we consider the ALV network of 2020s composed of three L-shaped interferometers operating at their design sensitivities and Einstein Telescope of 2030s made up of V-shaped interferometers. Ref. [29] investigated the capabilities of three to five-interferometer detector networks of 2020s in terms of their horizon distances to inspiralling BNSs and their sky-localization of these sources. Our work here is somewhat complementary in the sense that we are mostly concerned with how early the GW networks can detect the inspiral before the merger.

We compute the advance warning times via the following procedure: (i) We start with a GW source presumed to be an inspiralling BNS at a certain luminosity distance. (ii) We determine the frequency at which the source enters a given interferometer's bandwidth. (iii) We determine the detection time by computing the frequency at which the network's accumulated signal-to-noise ratio (SNR) for the BNS inspiral equals 15. (iv) We define the advance warning time, T_{AW} , to be the remaining inspiral time to the merger from the instant of detection. We repeat this procedure for BNSs at luminosity distances varying from 50 Mpc to 1 Gpc with the smaller values intended for the ALV network and the larger ones for Einstein Telescope. In order to more faithfully represent an interferometer network such as ALV — consisting of three separate interferometers which have different orientations and positions — we employ root-mean-square averages over sky-position and polarization angles, and assign the interferometers angle-averaged sensitivities.

Our computation for T_{AW} is based on the Newtonian evolution of a binary system composed of two point masses in a quasi-circular Keplerian orbit. The long-term dynamics is governed by the radiation reaction of the GW emission from the system due to the time variance of the quadrupole moment of the binary. Though the Newtonian (leading-order) treatment gives the inspiral time with better than 95% accuracy, we nonetheless supplement it with post-Newtonian corrections up to 3.5 post-Newtonian order (3.5PN) [14]. However, even that fails to provide an accurate depiction of the binary evolution in the strong-field regime, where speeds $\gtrsim 0.1c$. This is a very complex and complicated problem requiring fully numerical treatment formulated in terms of general relativistic, magnetohydrodynamic codes with neutrino transport running on large-scale computing clusters and taking up to millions of CPU hours (see Ref. [30] for a review, and Refs. [31–33] for the latest developments and references therein). Despite its failures, our quadrupole radiation driven Newtonian evolution is more than sufficient to provide reliable estimations of advance warning times. We support this claim in Sec. IV with an extensive list of computations showing how much each of our approximations affects the inspiral time.

Let us emphasize that this article is intended as a pedagogical introduction to gravitational-wave astronomy written at a level accessible to Ph.D. students, advanced undergraduates, and colleagues in astronomy and/or astrophysics who wish to learn more about the underlying physics. Be that as it may, even the experts might find our results motivating and exciting.

This article is organized as follows. Sec. II introduces the formulation for the leading-order evolution of the binary inspiral.

Sec. III details the interferometer response to GWs based on topology. Sec. IV lists the various idealizations we employ to simplify our treatment and supplies justification for each. Sec. V tests our model network and evolution using the parameters of GW170817 and the corresponding observations. Sec. VI contains our main results presented as advance warning times in Tables III, IV; and as horizon distances and event rates in Table V. In Sec. VII, we recompute the advance warning times in the case of black hole - neutron star inspirals to see whether or not future detectors can forecast a tidal disruption event, for which we summarize our findings in Table VI.

Throughout the text, f denotes the GW frequency of the dominant quadrupole mode, which is twice the orbital (Keplerian) frequency f_K . We employ the \simeq symbol when displaying the numerical values of quantities which we usually truncate at four significant digits. The \approx symbol is reserved for approximations whereas \sim denotes rough, order-of-magnitude equalities, e.g., $\pi \simeq 3.142$, $\pi \approx 3$, $\pi \sim \mathcal{O}(1)$. Overdots denote time derivatives with respect to detector-frame time, e.g., $\dot{E} = dE/dt$, and \propto denotes proportionalities. Unless otherwise noted, we use standard SI units.

II. Binary neutron star inspirals

A. Newtonian evolution

For us, the starting point for the evolution of a binary under gravitational radiation reaction is the expression for the power emitted in GWs given by the celebrated Einstein quadrupole formula [34]

$$\dot{E} = \frac{G}{5c^5} \langle \ddot{Q}_{ij} \ddot{Q}_{ij} \rangle. \quad (2.1)$$

Here, Q_{ij} is a trace-reversed mass quadrupole moment which is the dominant contribution to the power emitted by a system with changing mass moments.

Here, we are specifically interested in the motion of two point masses in a circular orbit around a common center of mass. Labelling the masses by $m_1 \leq m_2$, we have, for a binary in a circular orbit with Keplerian angular frequency Ω and separation r ,

$$\dot{E} = \frac{32}{5} \frac{G\mu^2}{c^5} r^4 \Omega^6, \quad (2.2)$$

where $\mu = m_1 m_2 / M$ is the reduced mass and $M = m_1 + m_2$ is the total mass. We justify our simplification of motion to circular orbits in Sec. IV.

An important quantity in GW astronomy is the chirp mass of the binary given by

$$M_c = \mu^{3/5} M^{2/5} = \frac{(m_1 m_2)^{3/5}}{(m_1 + m_2)^{1/5}}, \quad (2.3)$$

which turns Eq. (2.2) into

$$\dot{E} = \frac{32}{5} \frac{c^5}{G} \left(\frac{GM_c \omega}{2c^3} \right)^{10/3}, \quad (2.4)$$

where $\omega = 2\Omega$ is the angular frequency of the quadrupolar GWs. The quantity in parantheses in Eq. (2.4) is ubiquitous in post-Newtonian theory and is referred to as the dimensionless inverse separation x . As $x \propto v^2/c^2$, it is used to keep track of post-Newtonian orders and we can see from in Eq. (2.4) that $\dot{E} \propto x^5$.

The emission of power in GWs decreases the total energy of the binary given by

$$E_b = -\frac{Gm_1 m_2}{2r}. \quad (2.5)$$

$\dot{E}_b \propto \dot{r}/r^2$, so $\dot{E}_b < 0$ implies $\dot{r} < 0$, i.e, the orbital separation decreases making the orbit more bound in time. Using Kepler's

third law, $\Omega^2 = GMr^{-3}$, and Eq. (2.3) we obtain

$$E_b = - \left(\frac{G^2 M_c^5 \omega^2}{32} \right)^{1/3}. \quad (2.6)$$

Energy conservation dictates that $\dot{E} = -\dot{E}_b$. Using the chain rule to determine \dot{E}_b from Eq. (2.6) and setting the resulting expression equal to Eq. (2.4) yields $\dot{\omega}$ as a function of ω and various constants. Translating this expression using $\omega = 2\pi f$ we arrive at the standard expression for the GW frequency evolution

$$\dot{f} = \frac{96}{5} \pi^{8/3} \frac{(GM_c)^{5/3}}{c^5} f^{11/3} \quad (2.7)$$

This can be integrated straightforwardly after defining a new time variable $\tau \equiv t_{\text{coal}} - t$ that equals zero when the neutron stars coalesce. Using τ we can now define an inspiral time at a given GW frequency

$$\tau_{\text{insp}}(f) = \frac{5}{256\pi} \frac{c^5}{(\pi GM_c)^{5/3}} f^{-8/3}, \quad (2.8)$$

which we can rewrite as follows

$$\tau_{\text{insp}}(f) \simeq 16.72 \text{ minutes} \left(\frac{1.219 M_\odot}{M_c} \right)^{5/3} \left(\frac{10 \text{ Hz}}{f} \right)^{8/3}, \quad (2.9)$$

where $1.219 M_\odot$ is the chirp mass corresponding to $m_1 = m_2 = 1.4 M_\odot$.

We can also compute the number of GW cycles over the course of an inspiral. Given that the orbital period $T_K(t)$ varies over a time scale much larger than T_K itself we can write

$$\mathcal{N}_{\text{cyc}}(f) = \int_f^{f_{\text{max}}} \frac{f'}{\dot{f}'} df' = \frac{1}{32\pi} \frac{c^5}{(\pi GM_c)^{5/3}} \left[f^{-5/3} - f_{\text{max}}^{-5/3} \right] \quad (2.10)$$

We now introduce a cut-off for the inspiral imposed by the frequency of the innermost stable circular (ISCO) orbit in Schwarzschild spacetime

$$\Omega_{\text{ISCO}} = \frac{c^3}{6^{3/2} GM}. \quad (2.11)$$

We will see in Sec. IV that $f_{\text{ISCO}} \sim 1000 \text{ Hz}$ for a system with $M \approx 2 M_\odot$. On the other hand, the frequencies of interest for our advance warning time estimations will be $\lesssim 10 \text{ Hz}$ meaning that $f^{-5/3} \gg f_{\text{ISCO}}^{-5/3}$. Therefore, at the leading (Newtonian) order, the number of GW cycles can be approximated by

$$\mathcal{N}_{\text{cyc}}(f) \approx \frac{1}{32\pi} \frac{c^5}{(\pi GM_c)^{5/3}} f^{-5/3} \quad (2.12)$$

which can be rewritten as

$$\mathcal{N}_{\text{cyc}}(f) \approx 1.605 \times 10^4 \left(\frac{10 \text{ Hz}}{f} \right)^{5/3} \left(\frac{1.219 M_\odot}{M_c} \right)^{5/3}. \quad (2.13)$$

This expression is quite telling: if a ground-based interferometer picks up an inspiralling BNS at $f = 10 \text{ Hz}$ then there will be $\gtrsim \mathcal{O}(10^4)$ GW cycles in the detector's data stream until the merger.

Another useful relation is how the inspiral time scales with respect to the orbital radius corresponding to the observed GW frequency. From Kepler's third law, we immediately have $\dot{r}/r = -2\dot{\Omega}/(3\Omega) = -2\dot{f}/(3f)$, which, via Eq. (2.8), yields

$\dot{r}/r = -1/(4\tau)$ which integrates to

$$r(\tau) = r_i \left(\frac{\tau}{\tau_i} \right)^{1/4}, \quad (2.14)$$

where $r_i, \tau_i = t_{\text{coal}} - t_i$ are the initial radius and time that the BNS is “picked up” by a detector. Solving $\tau(f_i) = \tau_i$ for $f_i = \Omega_i/\pi$ using Eq. (2.8) and rewriting Ω_i as a function of r_i via Kepler’s third law gives us

$$\tau_i = \frac{5}{256} \frac{c^5 r_i^4}{G^3 M^2 \mu} \simeq 20.37 \text{ hours} \left(\frac{T_K}{1 \text{ s}} \right)^{8/3} \left(\frac{2.8 M_\odot}{M} \right)^{2/3} \left(\frac{0.7 M_\odot}{\mu} \right), \quad (2.15)$$

where the seemingly arbitrary $0.7 M_\odot$ is the value of μ for $m_1 = m_2 = 1.4 M_\odot$.

Let us now turn our attention to the GWs generated by the inspiral. These are tensorial perturbations propagating at the speed of light in flat (Minkowski) spacetime. In the so-called wave zone, defined by the condition $c/f \ll D$, where D is the distance to the GW source, these tensor modes satisfy the flat spacetime sourceless wave equation. In a suitable gauge, such as the commonly used transverse-traceless gauge, it can be shown that there exist only two physical degrees of freedom which manifest themselves as two independent polarization amplitudes h_+ and h_\times . For a binary in a circular orbit, these states read

$$h_+(t) = h_c(t) \left(\frac{1 + \cos^2 \iota}{2} \right) \cos[\Phi_N(t)], \quad (2.16)$$

$$h_\times(t) = h_c(t) \cos \iota \sin[\Phi_N(t)], \quad (2.17)$$

where

$$h_c(t) = \frac{4}{D} \left(\frac{GM_c}{c^2} \right)^{5/3} \left(\frac{\pi f(t)}{c} \right)^{2/3} \quad (2.18)$$

is the characteristic strain and $\iota = \cos^{-1}(\hat{\mathbf{n}} \cdot \hat{\mathbf{L}})$ is the inclination angle between the line of sight unit vector $\hat{\mathbf{n}}$ and the orbital angular momentum unit vector $\hat{\mathbf{L}}$. For an orbit seen edge on, $\iota = \pi/2$ giving $h_\times = 0$, i.e., a purely plus-polarized wave. When $\iota = 0$ the orbit is seen face-on and we have a circularly-polarized wave: $\langle h_+ \rangle = \langle h_\times \rangle$ where $\langle \dots \rangle$ denote time-averages over one orbit. Note that as f increases in time, so does $h(t)$ hence the characteristic “chirping” of GW signals.

$\Phi_N(t)$ in Eqs. (2.16, 2.17) is the phase of the GWs given by

$$\begin{aligned} \Phi_N(t) &= \int_{t_i}^t dt' \omega(t') \\ &= -2 \left(\frac{5GM_c}{c^3} \right)^{-5/8} (t_{\text{coal}} - t)^{5/8} + \Phi_0, \end{aligned} \quad (2.19)$$

where $\Phi_0 \equiv \Phi(t = t_{\text{coal}})$ is an integration constant. The subscript N denotes the Newtonian (leading-order) contribution. Higher-order contributions can be added in terms a post-Newtonian series, which make up to $\lesssim 2\%$ of the total phase. Although we will include contributions up to and including 3.5PN to obtain the results of Sec. VI, we will not show these expressions here, but they can be found in Ref. [14].

The nomenclature “plus” (+) and “cross” (×) follows from the effects that passing GWs have on the plane transverse to their direction of propagation. If we were to conceive of a “toy” detector made up of a circular configuration of test-masses lying in the x - y plane, a GW propagating along the z direction would stretch/compress the circular arrangement in a + and × pattern with a 90° phase difference. This is the manifestation of the tidal strain of the GWs on the tranverse plane. Next, let us briefly explore how an actual detector, i.e., an interferometer, responds to passing GWs.

III. Interferometer response to gravitational waves

A. LIGO-Virgo configuration: L-shaped topology

We start by first considering the L-shaped interferometer topology dating back to Michelson [35]. Although the GWs are described by propagating tensor modes, an interferometer (IFO) can only measure a scalar quantity known as the response function (or GW strain) which is a linear combination of the polarizations given by

$$h(t) = F_+(\theta, \phi, \psi) h_+(t) + F_\times(\theta, \phi, \psi) h_\times(t), \quad (3.1)$$

where

$$F_+ = \frac{1}{2} (1 + \cos^2 \theta) \cos 2\phi \cos 2\psi - \cos \theta \sin 2\phi \sin 2\psi, \quad (3.2)$$

$$F_\times = \frac{1}{2} (1 + \cos^2 \theta) \cos 2\phi \sin 2\psi + \cos \theta \sin 2\phi \cos 2\psi \quad (3.3)$$

are the antenna pattern functions of the detectors; θ, ϕ are the sky coordinates; and ψ is an additional angle coming from the respective rotations of detectors' frames to source frame. We can't apriori know θ, ϕ, ψ , however, we can extract their values with some limited precision over the course of an inspiral. The longer the inspiral stays in the detector bandwidth, the better we can estimate these angles. In the case of GW170817 which swept the ALV network over roughly 3000 GW cycles, the source sky localization was 28 deg^2 using data from three IFOs [5]. For our estimations, we employ suitable averages of these angles as explained below. For details on how to obtain Eqs. (3.2, 3.3) see, e.g., Sec. 4.2.1 of Ref. [36].

To compute the advance warning times we need to know how “loud” the binaries become as they sweep across the IFO's detection bandwidth. This is given by the signal-to-noise ratio (SNR) of the GWs in the detectors' bandwidth. The SNR is computed in the frequency domain so we Fourier-transform the time-domain strains of Eqs. (2.16) and (2.17) to obtain

$$\tilde{h}_+(f) = A \frac{c}{D} \left(\frac{GM_c}{c^3} \right)^{5/6} e^{i\Psi_+(f)} \frac{1}{f^{7/6}} \frac{1 + \cos^2 \iota}{2}, \quad (3.4)$$

$$\tilde{h}_\times(f) = A \frac{c}{D} \left(\frac{GM_c}{c^3} \right)^{5/6} e^{i\Psi_\times(f)} \frac{1}{f^{7/6}} \cos \iota, \quad (3.5)$$

where $A = \pi^{-2/3} \sqrt{5/24}$. Explicit expressions for $\Psi_{+, \times}$ show that they are out of phase by $\pi/2$ (the details of the Fourier transformation can be found in Sec. 4.5 of Ref. [37]). Accordingly, the Fourier transform of the detector strain (3.1) is given by

$$\tilde{h}(f) = A \frac{c}{D} \left(\frac{GM_c}{c^3} \right)^{5/6} f^{-7/6} e^{i\Psi_N} Q(\theta, \phi, \psi, \iota), \quad (3.6)$$

where

$$Q(\theta, \phi, \psi, \iota) = F_+(\theta, \phi, \psi) \frac{1 + \cos^2 \iota}{2} + i F_\times(\theta, \phi, \psi) \cos \iota, \quad (3.7)$$

is the quality factor. The i in front of F_\times in $Q(\theta, \phi, \psi, \iota)$ is due to the $\pi/2$ phase difference between $+$ and \times modes. Ψ_N is the leading-order contribution to the frequency-domain phase

$$\Psi_N = \Psi_+(f)|_N = 2\pi f(t_{\text{coal}} + D/c) - \Phi_0 - \frac{\pi}{4} + \frac{3}{128} \left(\pi f \frac{GM_c}{c^3} \right)^{-5/3}. \quad (3.8)$$

Higher-order contributions up to and including 3.5PN can be found in Ref. [36].

The detection criterion we employ here is quantified in terms of the optimal SNR defined by

$$\rho = \left[\int_0^\infty d \ln f \frac{|2\tilde{h}(f)\sqrt{f}|^2}{S_n(f)} \right]^{1/2}, \quad (3.9)$$

where $\sqrt{S_n(f)}$ is the *amplitude spectral density* (ASD) of the detector (also called spectral strain sensitivity, or simply, detector noise). It is usually this quantity that is shown in a typical interferometer strain sensitivity plot with the characteristic strain, $|\tilde{h}(f)\sqrt{f}|$, due to various GW sources overlaid for comparison. We show such plots in Secs. V and VI.

Substituting Eq. (3.6) into Eq. (3.9) yields

$$\rho^2 = \frac{5}{6} \pi^{-4/3} \frac{c^2}{D^2} \left(\frac{GM_c}{c^3} \right)^{5/3} |Q(\theta, \phi, \psi, \iota)|^2 \int_0^{f_{\text{ISCO}}} df \frac{f^{-7/3}}{S_n(f)}, \quad (3.10)$$

where we truncate the integral at the cut-off frequency of the inspiral $f_{\text{ISCO}} = \Omega_{\text{ISCO}}/\pi$.

It remains to compute $|Q(\theta, \phi, \psi, \iota)|^2$. Since we can not a priori know the direction of the source, it is appropriate to average over the angles $\theta, \phi, \psi, \iota$ which we compute via the following RMS-averaging integral

$$\langle F_+^2 \rangle \equiv \frac{1}{2\pi} \int_0^{2\pi} d\psi \frac{1}{4\pi} \int_0^{2\pi} d\phi \int_0^\pi d\theta \sin \theta F_+^2(\theta, \phi, \psi) = \frac{1}{5} \quad (3.11)$$

and likewise $\langle F_\times^2 \rangle = 1/5$. Finally, we average over the orbital inclination angle

$$\frac{1}{2} \int_{-1}^1 d(\cos \iota) \left[\left(\frac{1 + \cos^2 \iota}{2} \right)^2 + \cos^2 \iota \right] = \frac{4}{5}. \quad (3.12)$$

Thus we have that

$$\langle |Q(\theta, \phi, \psi, \iota)|^2 \rangle_{\theta, \phi, \psi, \iota} = \frac{4}{25}. \quad (3.13)$$

As angles have zero averages in general, we can think of the RMS as the standard deviation ($\sigma = 2/5$).

In a network of N interferometers, the total SNR is defined as follows

$$\rho_{\text{tot}} = \left[\sum_{i=1}^N \rho_i^2 \right]^{1/2}, \quad (3.14)$$

where Eq. (3.10) is employed to compute ρ_i^2 of individual interferometers each with a specific quality factor Q_i . Here, instead of working with specific quality factors of the LIGO and the Virgo interferometers, we consider a *model network* of three IFOs ($N = 3$), where one is near-optimally oriented/positioned with $|Q| = 2\sigma = 4/5$. The second IFO operates at the RMS average; thus it has $|Q| = 2/5$. It remains to assign a quality factor to the third IFO. We wish to make this operate below the RMS average, but it would be pointless to simply set $Q = 0$. We therefore somewhat arbitrarily set $\psi = 0, \iota = 0$ and introduce the following θ, ϕ -only averages

$$\langle F_+^2 \rangle_{\theta, \phi} = \frac{7}{30}, \quad \langle F_\times^2 \rangle_{\theta, \phi} = \frac{1}{6} \quad (3.15)$$

yielding

$$\langle |Q(\theta, \phi, \psi = 0, \iota = 0)|^2 \rangle_{\theta, \phi} = \frac{2}{5}. \quad (3.16)$$

Using this value, we assign our below-average third IFO $|Q| = 4/5 - \sqrt{2/5} \simeq 0.1675$. This may seem somewhat ad hoc, but it is our way of representing the response of a three-IFO network to a single source. In other words, we map the three different IFO responses due to a single source to a single IFO's response to three different sources differing in amplitudes from the optimal case by quality factors $|Q_i| = 4/5, 2/5$, and $4/5 - \sqrt{2/5}$. Accordingly, we now introduce the norm of the frequency-domain strain (3.6)

$$\tilde{H}_i(f) \equiv \tilde{A}_i h_0 f^{-7/6} \quad (3.17)$$

for each IFO labelled by i , where

$$h_0 = \frac{c}{D} \left(\frac{GM_c}{c^3} \right)^{5/6} \quad (3.18)$$

and $\tilde{A}_i \equiv A|Q_i|$ are given in Table I. The SNR for each interferometer can now be written as

$$\rho_i = 2\tilde{A}_i h_0 \left[\int_0^{f_{\text{ISCO}}} df \frac{f^{-7/3}}{S_n(f)} \right]^{1/2}. \quad (3.19)$$

We arbitrarily make the following assignments for our network: $h = 1, m = 2, l = 3$ representing high, medium, low signal strain at IFO $_i$, respectively. We summarize our network in the following table.

IFO $_i$	$ Q_i $	\tilde{A}_i	$\tilde{H}_i(f)$	IFO response
1	$\frac{4}{5}$	$\frac{4}{5}A$	$\frac{4}{5}Ah_0 f^{-7/6}$	high (h)
2	$\frac{2}{5}$	$\frac{2}{5}A$	$\frac{2}{5}Ah_0 f^{-7/6}$	medium (m)
3	$\frac{4}{5} - \sqrt{\frac{2}{5}}$	$\left(\frac{4}{5} - \sqrt{\frac{2}{5}}\right)A$	$\left(\frac{4}{5} - \sqrt{\frac{2}{5}}\right)Ah_0 f^{-7/6}$	low (l)

TABLE I. Our model for the Advanced-LIGO-Virgo network ca. 2020. Column two shows the quality factor Q_i for each IFO and column three the corresponding amplitude scalar \tilde{A}_i introduced in Eq. (3.17). Column four lists the magnitude of the frequency-domain strain at each IFO via Eq. (3.17). The last column shows how loud the GW strain is at a given IFO due source sky position and IFO orientation. Recall $A = \pi^{-2/3} \sqrt{5/24}$. Maximum value for $|Q_i|$ is 1, and minimum is 0.

We can now write the total SNR for our three L-IFO network

$$\rho_{\text{tot}} = \sqrt{\rho_h^2 + \rho_m^2 + \rho_l^2} \quad (3.20)$$

with ρ_h, ρ_m, ρ_l given by Eq. (3.19) and Table I.

B. Einstein Telescope configuration: triangular topology

Current design of Einstein Telescope (ET) is based on a [equilateral] triangular configuration with 10 km armlengths [20]. Within this equilateral triangle, ET will consist of three V-shaped cryogenic interferometers housed underground to significantly reduce seismic and gravity-gradient noises [20]. This closed topology will allow the detector to form a null stream completely devoid of a signal [38], which can be used to rule out spurious events [39]. Additionally, as we show below, the response function and the quality factor of the triangular configuration are independent of the azimuthal angle ϕ hence ET will have no blind spots [40]. However, the 60° arm separation reduces the strain sensitivity of a V-shaped interferometer by a factor of $\sin 60^\circ = \sqrt{3}/2$ compared to an L-shaped interferometer with the same armlength. So for a single V-IFO the antenna patterns of (3.2, 3.3) become

$$F_+^1(\theta, \phi, \psi) = \frac{\sqrt{3}}{2} F_+(\theta, \phi, \psi), \quad F_\times^1(\theta, \phi, \psi) = \frac{\sqrt{3}}{2} F_\times(\theta, \phi, \psi), \quad (3.21)$$

where the superscript 1 labels one of the three V's of the triangle. Since the other two V-IFOs lie in the same plane as the first one, their antenna patterns can be obtained simply by rotating in the azimuthal direction by $120^\circ, 240^\circ$, respectively

$$F_{+, \times}^2(\theta, \phi, \psi) = F_{+, \times}^1(\theta, \phi + 2\pi/3, \psi), \quad (3.22)$$

$$F_{+, \times}^3(\theta, \phi, \psi) = F_{+, \times}^1(\theta, \phi - 2\pi/3, \psi). \quad (3.23)$$

The individual antenna responses combine to cancel the ϕ and ψ dependence of the total power pattern

$$F_\Delta^2 \equiv \sum_{A=1}^3 (F_+^A)^2 + (F_\times^A)^2 = \frac{9}{32} (1 + 6 \cos^2 \theta + \cos^4 \theta). \quad (3.24)$$

From this, we immediately have that the RMS average is given by $\langle F_\Delta^2 \rangle^{1/2} = 3/\sqrt{10}$ and the minimum value is $F_\Delta(\pi/2) = 3/\sqrt{32}$; thus a triangular detector made-up of three V-IFOs has all-sky coverage.

For the total SNR accumulated in a triangular detector we have

$$\begin{aligned} \rho_{\text{tot},\Delta}^2 &= \sum_{A=1}^3 \rho_A^2 \\ &= \frac{5}{6} \pi^{-4/3} h_0^2 |Q(\theta, \phi, \psi, \iota)|_\Delta^2 \int_0^{f_{\text{ISCO}}} df \frac{f^{-7/3}}{S_n(f)}, \end{aligned} \quad (3.25)$$

where

$$|Q(\theta, \phi, \psi, \iota)|_\Delta^2 = \sum_{A=1}^3 (F_+^A)^2 \frac{1 + \cos^2 \iota}{2} + (F_\times^A)^2 \cos \iota \quad (3.26)$$

which is independent of ϕ [40]. We once again take the RMS average of this quantity

$$\bar{Q}_\Delta^2 \equiv \langle |Q(\theta, \phi, \psi, \iota)|_\Delta^2 \rangle_{\theta, \phi, \psi, \iota} = \frac{9}{25} \quad (3.27)$$

which is larger than a single L-shaped IFO's RMS average of 4/25 given in Eq. (3.13).

As we can not a priori know the source sky position or orientation we will model the response of ET using the RMS-averaged SNR

$$\rho_{\text{tot},\Delta} = \frac{6}{5} A h_0 \left[\int_0^{f_{\text{ISCO}}} df \frac{f^{-7/3}}{S_n(f)} \right]^{1/2}, \quad (3.28)$$

where h_0 is given by Eq. (3.18) and $A = \pi^{-2/3} \sqrt{5/24}$ as before. Accordingly, we define an RMS-averaged frequency-domain strain

$$\begin{aligned} \tilde{H}_\Delta(f) &\equiv A \bar{Q}_\Delta h_0 f^{-7/6} \\ &= \frac{1}{2} \sqrt{\frac{3}{10}} \frac{c}{D} \left(\frac{GM_c}{c^3} \right)^{5/6} f^{-7/6}. \end{aligned} \quad (3.29)$$

This is ET's sky-averaged response to a BNS inspiral at luminosity distance D and chirp mass M_c . Thus, $\tilde{H}_\Delta(f)$ is like the $\tilde{H}_i(f)$ of Table I, but different in that $\tilde{H}_\Delta(f)$ represents the total response of the entire three V-IFO network whereas $\tilde{H}_i(f)$ is the response of the i^{th} L-IFO.

In Sec. VI we will consider BNS systems inspiralling at varying luminosity distances as typical sources for the ALV and ET networks. To compute the resulting SNRs, we will slightly modify the integrals in Eqs. (3.19, 3.28) and use design sensitivities of A-LIGO and ET's B and C configurations for $\sqrt{S_n(f)}$. Before we present our results, we list the various idealizations that we have adopted to simplify our computations. For each idealization we present an estimated error. Our overall conclusion is that our simplifications do not significantly change our estimations of advance warning times.

IV. Simplifications and idealizations used in evolving the inspiral

1. *Neglecting strong-field gravity.* As our aim here is to provide a good order-of-magnitude estimation for the advance warning times, we model the neutron stars as point masses all the way to the merger. The point-particle treatment is severely inadequate for the strong-field evolution of the binary, but these systems spend only the last few seconds of the inspiral in this regime, e.g., the inspiral time from $f = 100$ Hz to the merger is $\tau_{\text{insp}}(f = 100 \text{ Hz}) \simeq 2.161$ seconds according to Eq. (2.8). And even at $f = 100$ Hz, a $m_1 = m_2 = 1.4 M_\odot$ neutron-star binary has separation $r \approx 155$ km, which translates to a dimensionless strength of gravity of $\approx 2.6\%$. This percentage is mostly accounted for by the post-Newtonian corrections to our Newtonian (leading order) evolution. Here, we will go up to 3.5pN for our advance warning time computations. Therefore, given that strong-field effects may at most change T_{AW} by a second, we can neglect them

for our purposes, but let us add that a faithful evaluation of BNS systems above $f \gtrsim 100$ Hz is a very active and important branch of general relativity and gravitational-wave astronomy.

2. *Truncating the inspiral at the Schwarzschild ISCO.* We artificially end the inspirals at the Schwarzschild ISCO of the BNS with coordinate radius $r_{\text{ISCO}} = 6GM/c^2$ and angular frequency Ω_{ISCO} given by Eq. (2.11) which translates to the following dominant-mode (quadrupole) GW frequency

$$f_{\text{ISCO}} = \frac{c^3}{6^{3/2}\pi GM} \simeq 1571 \text{ Hz} \quad (4.1)$$

for $M \equiv m_1 + m_2 = 2.8M_\odot$. The true ISCO is located at $r < r_{\text{ISCO}}$ with frequency possibly up to 1.7 kHz [41], however, there is no simple expression for it akin to Eq. (4.1) and its extraction from numerical simulations is a rather involved procedure. Therefore, we employ Eq. (4.1) as our cut-off for inspirals throughout this work.

3. *Setting $m_1 = m_2 = 1.4M_\odot$.* Let us briefly explore what the cost of setting $m_1 = m_2 = 1.4M_\odot$ is for our calculations. Including the error bars, the known range for neutron star masses runs from $\approx 0.5M_\odot$ to $\approx 3M_\odot$ with the actual values restricted between $\approx 1M_\odot$ and $\approx 2M_\odot$ [42] (one exception being J1748-2021B with mass $2.74^{+0.21}_{-0.21}M_\odot$ [43]). Of these measured masses, a subset comprised of double neutron stars, such as the famed Hulse-Taylor binary, have the smallest error bars with masses ranging from $\approx 1.2M_\odot$ to $\approx 1.5M_\odot$. Additionally, the masses involved in GW170817 are inferred to be between $1.17M_\odot$ and $1.60M_\odot$ [5]. Therefore, let us restrict the masses to lie between $1.2M_\odot$ and $1.6M_\odot$ then focus on the quantities of interest for us, which are the inspiral time (τ_{insp}), the frequency domain strain (\tilde{H}), and the frequency of the innermost stable circular orbit (f_{ISCO}) given by Eq. (4.1) above. We summarize how these scale in terms M_c, M , thus m_1, m_2 , in Table II below.

Quantity	Standard Scaling	Scaling in terms of m_1, m_2	Min \leq Value $_{1.4M_\odot} \leq$ Max
τ_{insp}	$M_c^{-5/3}$	$(m_1 m_2)^{-1} (m_1 + m_2)^{-1}$	$0.335 \leq 0.5 \leq 0.794$
\tilde{H}	$M_c^{5/6}$	$(m_1 m_2) (m_1 + m_2)^{3/2}$	$0.7834 \leq 0.891 \leq 0.996$
f_{ISCO}	M^{-1}	$(m_1 + m_2)^{-1}$	$0.4375 \leq 0.5 \leq 0.583$

TABLE II. The scaling of the physical quantities of interest in this article in terms the binary masses m_1, m_2 restricted to lie between $1.2M_\odot$ and $1.6M_\odot$. Value $_{1.4M_\odot}$ represents the value of the quantities in column three evaluated at $m_1 = m_2 = 1$ mass unit corresponding to $1.4M_\odot$.

The ranges in column four show that \tilde{H} changes roughly by $\pm 10\%$ across the $1.2M_\odot - 1.6M_\odot$ mass range whereas the variation in f_{ISCO} matters not as it affects the advance warning times by less than a second (see above). The inspiral time seems to be more sensitive to our chosen mass values as indicated by the $\sim \begin{smallmatrix} +60\% \\ -30\% \end{smallmatrix}$ variation in Table II. As our intent is to provide an estimation for advance warning times in terms of orders of magnitude, this variation is tolerable. Moreover, it seems that this variation tends to lengthen τ_{insp} more than shorten it thus our setting $m_1 = m_2 = 1.4M_\odot$ is more likely to underestimate T_{AW} than overestimate it which is something we can live with. So we set $m_1 = m_2 = 1.4M_\odot$ henceforth.

4. *Neglecting eccentricity.* We further simplify our treatment by considering only quasi-circular inspirals meaning that at any given instant, the orbit can be treated as circular with the corresponding Keplerian frequency $f_K = (GM/r^3)^{1/2}/(2\pi)$. It was Peters and Matthews who first showed that eccentric binaries circularize in the weak field [44]. Using $\dot{a} = \dot{a}(a, e), \dot{e} = \dot{e}(a, e)$ they obtained

$$a(e) = c_0 \frac{e^{12/19}}{1 - e^2} \left(1 + \frac{121}{304} e^2 \right)^{870/2299} \equiv c_0 g(e), \quad (4.2)$$

where a is the semi-major axis of the eccentric orbit and c_0 is a constant. For $e \ll 1$ we have $g(e) \approx e^{12/19}$, thus we may write $e \approx [a g(e_i)/a_i]^{19/12}$ for a system with initial parameters a_i, e_i . Let us apply this to the Hulse-Taylor binary pulsar [45, 46] to show that the BNS orbits circularize by the time they enter the interferometers' bandwidth. Letting $f = 1 \text{ Hz} = 2f_K$, i.e., $a \simeq 3352 \text{ km}$ and using the currently observed values $a_i \approx 1.95 \times 10^6 \text{ km}$ and $e_i \approx 0.617$, we obtain $e \approx 6 \times 10^{-5}$. Thus our setting $e = 0$ is very reasonable.

5. *Quasi-circularity.* This implies that the timescale for the orbital radius to decrease is much longer than the orbital timescale, i.e., $|\dot{r}| \ll r\Omega$ during the inspiral. From $\Omega^2 = GM/r^3$ we can straightforwardly obtain an expression for the ratio of radial speed to tangential speed

$$\frac{|\dot{r}|}{r\Omega} = \frac{2}{3} \frac{|\dot{\Omega}|}{\Omega^2}, \quad (4.3)$$

which translates the quasi-circularity condition above to $|\dot{\Omega}| \ll \Omega^2$ which, via Eq. (2.7), gives

$$\frac{\dot{\Omega}}{\Omega^2} = \frac{96}{5} \frac{(GM_c)^{5/3}}{c^5} \Omega^{5/3} \ll 1 \quad (4.4)$$

This expression yields $\dot{\Omega}/\Omega^2 \approx 5.5 \times 10^{-4}$ at $f = 100$ Hz, which, as shown above, is a few seconds before the merger so the quasi-circularity assumption seems to hold almost until the plunge at $f = f_{\text{ISCO}}$.

6. *Neglecting higher-order multipole moments.* Another reasonable question is how much our estimation of advance warning times is affected by neglecting higher-order contributions to the loss of energy coming from, e.g., the current quadrupole and the mass octupole moments. The power radiated by the current quadrupole (\dot{E}_{cur}) by a binary in a circular orbit is $\mathcal{O}(v^2/c^2)$ smaller than the dominant quadrupole-mode power emission. More precisely, we have [37]

$$\frac{\dot{E}_{\text{cur}}}{\dot{E}} = \frac{1215}{896} \frac{v^2}{c^2} \left(\frac{m_2 - m_1}{M} \right)^2 = \frac{1215}{896} \frac{(\pi GMf)^{2/3}}{c^2} \left(\frac{m_2 - m_1}{M} \right)^2. \quad (4.5)$$

At $f = 100$ Hz, the first two factors $\simeq 3.6 \times 10^{-2}$ for $M = 2.8M_\odot$ which tells us that even in the strong-field regime, the next-to-leading order contribution is two orders of magnitude smaller. The ratio in Eq. (4.5) is further suppressed by $(m_2 - m_1)/M^2$ which, for our idealized equal-mass system, yields zero, but if we consider $m_1 = 1.2M_\odot, m_2 = 1.6M_\odot$ then it gives $\approx 2 \times 10^{-2}$ hence the ratio in Eq. (4.5) $\lesssim 10^{-3}$. Thus, we can neglect the current-quadrupole radiation completely. In a similar fashion, it can be shown that the power radiated by the mass octupole ($\ell = 3$) scales the same way as in Eq. (4.5) with respect to the dominant mass quadrupole radiation, but is ~ 50 times smaller hence we can neglect it as well [37]. Higher moments are suppressed by higher factors of v^2/c^2 as can be shown using post-Newtonian theory. Thus, our exclusiveness to the mass-quadrupole radiation is justified.

7. *Neglecting neutron star spins.* It is generally believed that neutron stars do not have large enough angular momentum to impart detectable spin effects into the GWs emitted by the BNS inspirals. The dominant effect due to the spins is the spin-orbit (SO) precession which contributes to the energy flux at the 1.5PN order [$\mathcal{O}(v^3/c^3)$] with respect to the leading-order quadrupole \dot{E} of Eq. (2.2) [14]. Restricting to the case of $m_1 = m_2$ we obtain

$$\frac{\dot{E}_{\text{SO}}}{\dot{E}} \lesssim 4 \frac{G\Omega m}{c^3} \chi + \mathcal{O}\left(\frac{v^5}{c^5}\right), \quad (4.6)$$

where we introduced the dimensionless Kerr spin parameter $\chi \equiv S/(Gm^2)$ which, for a neutron star (NS) with spin S and mass m , can be written as

$$\chi = \frac{c}{G} \frac{I}{m^2} \frac{2\pi}{P}, \quad (4.7)$$

where P is the spin period, and $I = (2/5)mR^2\kappa$ is the moment of inertia of the NS with R being the radius of the NS and $\kappa \sim \mathcal{O}(1)$ an intrinsic constant (see, e.g., Sec. 6.2 of Ref. [47]). A rather compact NS with $m = 1.4M_\odot, R = 11$ km, $P = 10$ ms has $\chi \lesssim 0.05$ whereas the fastest observed NS spin $\lesssim 0.04$ [48]. Therefore, at $f = 100$ Hz, the first term on the right-hand-side of Eq. (4.6) gives $\approx 4 \times 10^{-4}$. On the other hand, the spin-spin effects contribute at $\mathcal{O}(v^4/c^4) \times \dot{E}$ hence $\lesssim \dot{E}_{\text{SO}}$. Thus, NS spins can be neglected for our estimation of advance warning times.

8. *Neglecting cosmological effects.* When we take into account the effects of the large-scale structure of the universe, many

quantities of interest are scaled by $(1+z)^\alpha$ where α is the appropriate power. The standard treatment adopts a Friedmann-Robertson-Walker cosmology with scale factor $a(t)$ and curvature $k = \pm 1$, or 0. Introducing the subscript s to denote quantities evaluated at the source frame, we have the following cosmological corrections

$$dt \rightarrow (1+z)dt_s, \quad (4.8)$$

$$f \rightarrow (1+z)^{-1}f_s \quad (4.9)$$

and the luminosity distance gets rescaled as

$$D \rightarrow (1+z)a(t)D. \quad (4.10)$$

Given that $\dot{f}_s = df_s/dt_s \sim f_s^{11/3}$, $h_s(t) \sim D^{-1}f_s^{2/3}$, and $\tau_{\text{insp},s} \sim f_s^{-8/3}$, the observed frequency evolution, the inspiral time, and the GW strain change according to

$$\dot{f} \sim (1+z)^{5/3}f^{11/3}, \quad (4.11)$$

$$\tau_{\text{insp}} \sim (1+z)^{-5/3}\tau_{\text{insp}}, \quad (4.12)$$

$$h(t) \sim (1+z)^{5/3}h(t). \quad (4.13)$$

Looking at Eqs. (2.7, 2.8, 2.18) we spot a common factor of $M_c^{5/3}$ in all of them. Therefore, we can accommodate the cosmological effects by introducing the redshifted chirp mass $\mathcal{M}_c \equiv (1+z)M_c$ which changes Eqs. (2.7, 2.8, 2.18) to

$$\dot{f} = \frac{96}{5}\pi^{8/3}\frac{(G\mathcal{M}_c)^{5/3}}{c^5}f^{11/3}, \quad (4.14)$$

$$\tau_{\text{insp}}(f) = \frac{5}{256\pi}\frac{c^5}{(\pi G\mathcal{M}_c)^{5/3}}f^{-8/3}, \quad (4.15)$$

$$h_c(t) = \frac{4}{D}\left(\frac{G\mathcal{M}_c}{c^2}\right)^{5/3}\left(\frac{\pi f}{c}\right)^{2/3}, \quad (4.16)$$

where f is the usual frequency in the observer/detector frame. So we see that the effects of the cosmological redshifting can be accounted for by the transformation $M_c \rightarrow \mathcal{M}_c$. This is because both \dot{f} and the GW amplitude are governed by the time scale GM_c/c^3 . Therefore, the inspiral evolves faster in the lab frame and we must now terminate it at a redshifted GW ISCO frequency which is less than f_{ISCO} of Eq. (4.1). On the other hand, the Fourier transform of $h_c(t)$ changes to

$$\tilde{H}(f) = A\frac{c}{D(1+z)}\left(\frac{G\mathcal{M}_c}{c^3}\right)^{5/6}f^{-7/6} \quad (4.17)$$

indicating that the frequency-domain strain in the detector frame decreases by a factor of $(1+z)^{-1/6}$. For the Advanced-LIGO-Virgo network, we consider a maximum value of 200 Mpc for D , which corresponds to $z \approx 0.02$ which redshifts f_{ISCO} by $\approx 2\%$ and reduces τ_{insp} by $\approx 7\%$. Therefore, we will neglect the effects of cosmological redshift when considering sources for the ALV network. On the other hand, for Einstein Telescope, we will go out to $D = 1$ Gpc $\Rightarrow z \approx 0.2$ which reduces τ_{insp} by $\sim 25\%$, thus we shall include the redshift effects in our computations of advance warning times and SNRs for which we provide the details in Sec. VI 2 (additional details can be found in, e.g., Ref. [49]).

V. GW170817 as a test of our model for the Advanced LIGO-Virgo network

On 17 August 2017, at 12:41:04 UTC, GWs from the inspiral and merger of a binary neutron star system swept the ALV network's frequency band from ≈ 30 Hz to ≈ 2000 Hz accumulating a total SNR of $\rho_{\text{tot}} = 32.4$ [5]. The inferred duration of the event in the network bandwidth was ≈ 57 seconds during which ≈ 3000 cycles of GW were emitted [50]. Assuming low-spin priors ($\chi \leq 0.05$, see point 7 of Sec. IV), the following values were inferred for the total mass, the chirp mass, and the luminosity

distance of the source with 90% confidence:

$$M = 2.74^{+0.04}_{-0.01} M_{\odot}, \quad M_c = 1.188^{+0.004}_{-0.002} M_{\odot}, \quad D = 40^{+8}_{-14} \text{ Mpc}. \quad (5.1)$$

Note that the error bar for the chirp mass is very small due to the fact that it can be extracted to high precision over thousands of GW cycles via Eq. (2.7).

How well does the “naive” Newtonian evolution based on the quadrupole formula perform? To test this, let us first compute the inspiral time, τ_{insp} , and the number of GW cycles, \mathcal{N}_{cyc} , for this BNS system with initial frequency $f_i = 30$ Hz and final frequency $f_{\text{ISCO}} \simeq 1605$ Hz. Eqs. (2.8) and (2.10) provide us with the leading-order values

$$\tau_{\text{insp}}^{\text{OPN}} \simeq 55.91 \text{ seconds}, \quad \mathcal{N}_{\text{cyc}}^{\text{OPN}} \simeq 2680. \quad (5.2)$$

If we wish to do better, we can add all of the known post-Newtonian contributions (up to 3.5PN²) resulting in

$$\tau_{\text{insp}}^{3.5\text{PN}} \simeq 56.65 \text{ seconds}, \quad \mathcal{N}_{\text{cyc}}^{3.5\text{PN}} \simeq 2711, \quad (5.3)$$

which more or less match the values above.

We now put our model three-IFO network to the test by computing the SNRs accumulated by each individual IFO and by the entire network. To do so, we take the best-inferred values for M, M_c, D from GW170817 given in Eq. (5.1) above and compute the SNRs $\rho_i, i = h, m, l$ via a slightly modified version of Eq. (3.19)

$$\bar{\rho}_i \equiv \rho_i(f_0, f_f) = 2\tilde{A}_i h_0 \left[\int_{f_0}^{f_f} df \frac{f^{-7/3}}{S_n(f)} \right]^{1/2}. \quad (5.4)$$

where $f_0 = 30$ Hz, $f_f = f_{\text{ISCO}}$ for GW170817 and \tilde{A}_i given in Table I. For this computation, we have neglected the cosmological corrections as 40 Mpc is in our “local” neighbourhood.

For $S_n(f)$ we use actual [noise-subtracted] LIGO-Livingstone (L1) data for GW170817 from LIGO’s website [52]. The data, sampled at 4096 Hz, is given as a discrete time series $h(t_i)$ for a duration of 2048 seconds in time steps of $\Delta t = 1/4096 \simeq 2.44 \times 10^{-4}$ seconds. We first Fourier-transform the data to frequency space and apply several high and low-frequency filters to isolate a window of $f \in [10, f_{\text{ISCO}}]$. The LIGO Open Science Center has a detailed Python-based tutorial on how to do this using the data from the very first GW detection (GW150914) [53]. We use a `Mathematica` based code developed at UCD to do the same for GW170817.

Fig. 1 shows our network. The red curve is L1’s ASD (sensitivity) during GW170817. We assume our three IFOs to identically have this sensitivity, but because their orientations and response functions differ, their sensitivity to a localized source is reduced. We represent this reduction by lowering the amplitude of the GW strain by appropriate quality factors ($|Q_i|$) explained in Sec. II and shown in Table I. The amplitude-adjusted strains $\tilde{H}_i(f)$ are represented by the dashed ($i = h$), solid ($i = m$), and dotted ($i = l$) lines in the figure where we actually plot $2\sqrt{f}\tilde{H}_i(f)$ as is standard. Using Eq. (5.4) we can immediately compute the SNRs accumulated by our network

$$\bar{\rho}_h = 29.2, \quad \bar{\rho}_m = 14.6, \quad \bar{\rho}_l = 6.11. \quad (5.5)$$

These are comparable to actual SNRs of L1, H1, and V1 for GW170817, which are, 26.4, 18.8, and 2.0, respectively³. The shaded region in Fig. 1 covers strains between $\tilde{H}_l(f)$ and $\tilde{H}_h(f)$. Given a randomly positioned/oriented BNS inspiral at 40 Mpc, we would in general expect a randomly oriented IFO’s response to lie in this shaded region.

² Although the equations of motion for circular orbits is now known up to 4PN [51], we are not aware of any publications explicitly showing the 4PN contributions to τ_{insp} and \mathcal{N}_{cyc} . Be that as it may, we suspect that a few PN experts have already obtained these.

³ At the time of GW170817, Virgo’s sensitivity had not reached the level of LIGO’s. Hence it accumulated a much smaller SNR for GW170817. By 2020, Virgo should be operating at nearly the same sensitivity of LIGO.

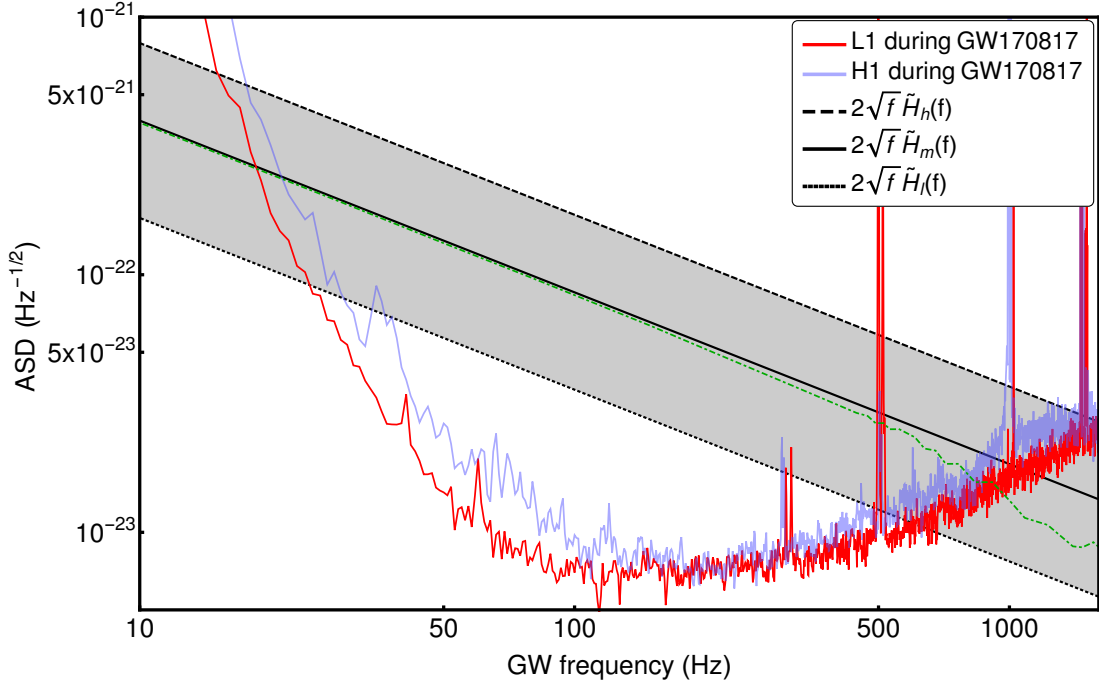


FIG. 1. GW170817 as it sweeps from 10 Hz to $f_{\text{ISCO}} \simeq 1605$ Hz across our network with ASD (sensitivity) of LIGO Livingstone (L1) during the event (the darker red curve). We also show the Hanford detector's sensitivity in light blue for comparison. The dashed, solid and dotted lines represent the frequency-domain GW strains ($2\sqrt{f}\dot{H}_i(f)$) with $i = h, m, l$ due to the inspiral of a binary neutron star system with parameters given in Eq. (5.1). The variation in strain amplitudes is the result of a given interferometer's orientation and the sky position of the source as explained in Sec. III A and summarized in Table I. More specifically, the dashed line is how “loud” GW170817 would appear in the data stream of an IFO with L1's sensitivity with near optimal orientation (quality factor $|Q| = 4/5 = 80\%$). Similarly, the solid line represents the strain in an identical inteferometer with $|Q| = 2/5 = 40\%$ (RMS-averaged response). Finally, the dotted line represents a pessimistic IFO orientation and source location (sub-optimal configuration) resulting in a reduction of $|Q|$ to $\simeq 16.7\%$. The shading represents the region of likelihood for the strain due to an inspiralling BNS with parameters of Eq. (5.1). In the case of a three-IFO network, we would expect all three strains to exist somewhere in the shaded region most of the time for an inspiral with GW170817's intrinsic parameters. The dot-dashed (green) curve shows a more realistic strain constructed with data from numerical simulations of Ref. [54] and rescaled to match our solid line at $f = 10$ Hz. The breakdown of the $\sqrt{f}f^{-7/6} = f^{-2/3}$ behavior of the strain around $f \sim 100$ Hz due to tidal effects is clear.

We can now compute the total SNR of GW170817 as inferred by our network

$$\bar{\rho}_{\text{tot}} = \sqrt{\bar{\rho}_h^2 + \bar{\rho}_m^2 + \bar{\rho}_l^2} = 32.6. \quad (5.6)$$

This matches the actual value of 32.4 very well. Therefore, we conclude that our model network performs well enough to act as our future ALV network of the 2020s once we change the ASD from the August 2017 value to design sensitivity.

VI. Results: Advance warning times for future binary neutron star inspirals

Our aim is to forecast GRBs using our model networks for the ALV era in the 2020s and the Einstein Telescope era in the 2030s. Our predictive capabilities depend on how much advance warning the future networks will give us prior to the merger/GRB. Our definition of advance warning is the inspiral time to the merger from a certain threshold instant \bar{t} at which point the network “agrees” that there is a GW transient statistically significant enough to issue warnings to electromagnetic telescopes. We define this threshold instant to be given at a frequency \bar{f} when the total SNR equals 15. More specifically, in the case of the ALV network, our statement is that there exists a frequency $\bar{f} < f_{\text{ISCO}}$ such that

$$\bar{\rho}_{\text{tot}} = \sqrt{[\rho_h(f_0^h, \bar{f})]^2 + [\rho_m(f_0^m, \bar{f})]^2 + [\rho_l(f_0^l, \bar{f})]^2} = 15, \quad (6.1)$$

where f_0^i are the initial GW frequencies at which a given inspiral enters the i^{th} IFO's sensitivity band, and are given by the solution set to

$$\sqrt{S_n(f_0^i)} = 2\sqrt{f_0^i \tilde{H}_i(f_0^i)}, \quad i = h, m, l \quad (6.2)$$

with $f_0^i < \bar{f}$. Once we know \bar{f} , we can compute the remaining time to the merger, $\tau_{\text{insp}}(\bar{f})$, using Eq. (2.8) and its 3.5PN-enhanced version from Ref. [14]. This is what we call our advance warning time T_{AW} . For simplicity, we set $m_1 = m_2 = 1.4M_\odot \implies M_c \simeq 1.219M_\odot$, which we justified in Point 3 of Sec. IV. With the masses fixed, the only remaining variable is the luminosity distance D . For the ALV network, we consider $D = 50, 100, 200$ Mpc as A-LIGO horizon will be slightly over 200 Mpc and A-Virgo's around 130 Mpc. For each value of D , we compute \bar{f} from Eq. (6.1) with which we then compute $T_{\text{AW}} = \tau_{\text{insp}}(\bar{f})$. We summarize our procedure in the flow diagram below.

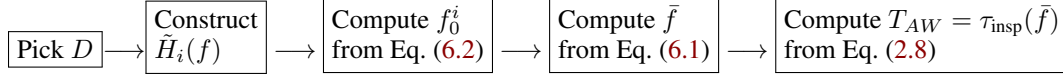


FIG. 2. Flow diagram summarizing our procedure for computing advance warning times T_{AW} with the Advanced-LIGO-Virgo network. We compute T_{AW} for BNS systems with $M = 2.8M_\odot$ inspiralling at $D = 50, 100, 200$ Mpc.

We additionally calculate the total accumulated SNR from f_0 to f_{ISCO} for each inspiral using

$$\bar{\rho}_F \equiv \sqrt{[\rho_h(f_0^h, f_{\text{ISCO}})]^2 + [\rho_m(f_0^m, f_{\text{ISCO}})]^2 + [\rho_l(f_0^l, f_{\text{ISCO}})]^2}. \quad (6.3)$$

We will introduce the corresponding expressions for ET in Sec. VI 2. To compute the SNRs defined above for the ALV network we require IFO noise data for which we use the ASD for the BNS-optimized A-LIGO design sensitivity expected to be attained ca. 2020 from Ref. [55], which is plotted as the thick solid (red) curve in Fig. 3. Sweeping across the detector's frequency band are RMS-averaged GW strains (\tilde{H}_m) due to BNS inspirals at $D = 50, 100, 200$ Mpc plotted from top to bottom, respectively (recall we plot $2\sqrt{f}\tilde{H}_i$ against detector noise). Each RMS-averaged strain is accompanied by its shaded region ranging from a near-optimally oriented strain (\tilde{H}_h) to a sub-optimally oriented strain (\tilde{H}_l) which were explained in Sec. V and first shown in Fig. 1. The height of a given strain above the detector sensitivity provides a good *visual* estimation for the corresponding SNR, but the reader should keep in mind that the actual computation involves the integral of a ratio, not a difference [cf. Eq. (3.9)].

1. Forecasting GRBs in the 2020s with the Advanced LIGO-Virgo Network

The advance warning time computation follows the procedure outlined in Fig. 2. We use numerical root finding to determine \bar{f} and f_0^i for all three values of D . The computation of SNRs and T_{AW} is then straightforward. We summarize our results in Table III where we present both the 0PN and the 3.5PN results for the advance warning times T_{AW} . As can be seen from the values for T_{AW} in the table, we can at best expect 85 seconds of early warning time. This time increases to approximately two minutes in the case of another GW170817-like event with $D = 40$ Mpc. We can estimate the likelihood of such an event happening again using the current best estimate for the BNS inspiral rate inferred from the O1 and O2 observing periods of Advanced LIGO: $R = 1540^{+3200}_{-1220} \text{ Gpc}^{-3}\text{yr}^{-1}$ [5]. This translates to ≈ 0.1 event per $(40\text{-Mpc})^3$ per year with the upper limit ≈ 0.3 . So we can at best hope to detect one 40-Mpc inspiral per a three-year period. Given that we might at best have a couple of minutes of warning time for a once-a-decade event, we do not expect to be able forecast GRBs in the Advanced LIGO-Virgo era. Be that as it may,

D (Mpc)	\bar{f} (Hz)	T_{AW}^{0PN} (sec)	$T_{\text{AW}}^{3.5PN}$ (sec)	$\bar{\rho}_F$
50	≈ 25.3	84.25	85.86	70.3
100	≈ 41.6	22.39	22.86	35.2
200	≈ 121	1.291	1.300	17.6

TABLE III. The ALV network's potential for providing advance warning times, T_{AW} , to electromagnetic observatories for the case of $m_1 = m_2 = 1.4M_\odot$ BNS inspirals at luminosity distances of $D = 50, 100, 200$ Mpc. \bar{f} is the frequency at which the SNR accumulated by the network reaches 15. $\bar{\rho}_F$ is the total accumulated network SNR. We present both the Newtonian (0PN) and the 3.5PN result for the advance warning times.

the ALV network will accumulate impressive SNRs (see $\bar{\rho}_F$ in Table III) for BNS inspirals out to 100 Mpc. As the measurement

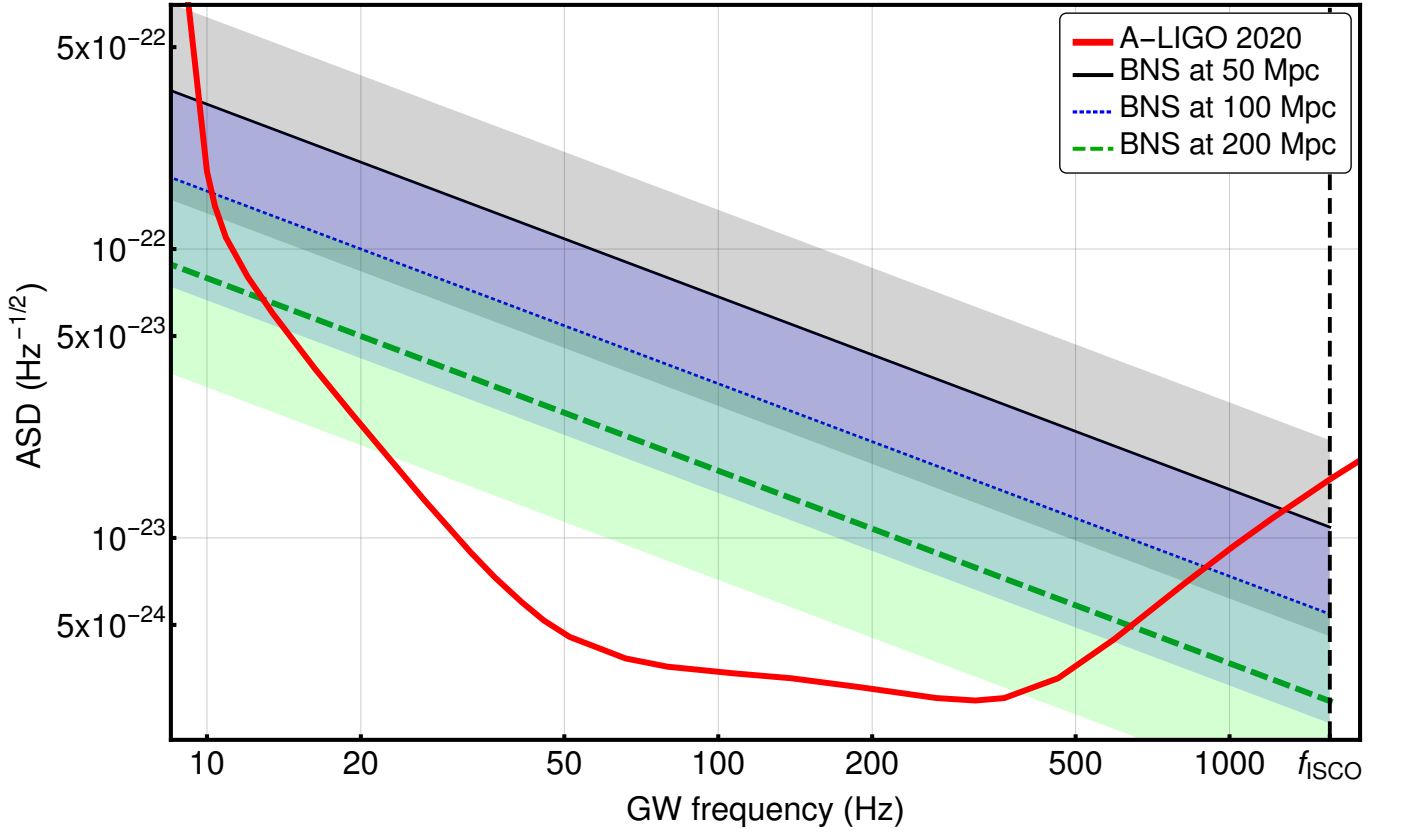


FIG. 3. Typical $m_1 = m_2 = 1.4M_\odot$ BNS inspirals sweeping across the Advanced LIGO-Virgo network in the 2020s. These may be the harbingers of short-hard GRBs. The solid (black), dotted (blue), and dashed (green) lines are the RMS-averaged strains ($2\sqrt{f}\tilde{H}_m$) at luminosity distances of $D = 50, 100, 200$ Mpc, respectively. The accompanying shaded regions span from the near-optimally oriented IFO ($2\sqrt{f}\tilde{H}_h$) to sub-optimally oriented IFO ($2\sqrt{f}\tilde{H}_l$) as explained in Fig. 1. The vertical dashed (black) line marks the ISCO frequency $f_{\text{ISCO}} \simeq 1571$ Hz at which point we terminate the inspirals.

errors for the system parameters are proportional to $\bar{\rho}_F^{-1}$ [56], inspirals that yield high SNRs ($\bar{\rho}_F \gtrsim 40$) will enable (i) high precision measurements of M_c, M [57]; (ii) source sky localization to $\lesssim 5 \text{ Deg}^2$ [58]; (iii) $\lesssim 10\%$ precision in the inferred NS masses [58] and the effective spin parameter χ_{eff} [59]; and (iv) restrictions on the equation of state and the tidal deformability parameters of neutron stars [54, 60–62]. We should caution the reader that such high-SNR systems will make up $\lesssim 1\%$ of the population of BNSs detected by the ALV network [38].

2. Forecasting GRBs in the 2030s using the Einstein Telescope

We now wish to quantify the forecasting capabilities of Einstein Telescope. To this end, we consider the inspiral of BNS systems at luminosity distances of 100, 200, 400, 1000 Mpc entering the ET band. These correspond to cosmological redshifts of $z \approx 0.0222, 0.0437, 0.085, 0.198$, respectively. To compute these, we used a flat Λ CDM model ($\Omega_k = 0$) with the latest Planck satellite parameters: $\Omega_\Lambda = 0.6911, \Omega_m = 0.3089, H_0 = 67.74 \text{ km s}^{-1} \text{ Mpc}^{-1}$ [63]. It is then straightforward to translate D to z (cf. Ref. [64]).

The SNR accumulated in ET from each inspiral is obtained by a modification to Eq. (3.28)

$$\bar{\rho}_{\text{ET}}(f_0, f) \equiv \frac{6}{5} A h_0 (1+z)^{-1/6} \left[\int_{f_0}^f df' \frac{f'^{-7/3}}{S_n^{\text{ET}}(f')} \right]^{1/2}, \quad (6.4)$$

where f_0 is the GW frequency at which the emitted GWs enter ET's detection band, i.e. $f_0 < f_{\text{ISCO}}$ such that

$$\sqrt{S_n^{\text{ET}}(f_0)} = 2\sqrt{f_0} \tilde{H}_{\text{ET}}(f_0) \quad (6.5)$$

with $\tilde{H}_{\text{ET}}(f)$ given by the redshifted version of Eq. (3.29)

$$\tilde{H}_{\text{ET}}(f) = \frac{1}{2} \sqrt{\frac{3}{10}} \frac{c}{D} \frac{1}{(1+z)} \left(\frac{G\mathcal{M}_c}{c^3} \right)^{5/6} f^{-7/6}, \quad (6.6)$$

where recall $\mathcal{M}_c = (1+z)M_c$. For the detector noise $\sqrt{S_n^{\text{ET}}(f)}$, we adopt the ASD for the B and C configurations known as ET-B and ET-C, respectively [65], which we plot as the solid dark (red) and light (brown) curves in Fig. 4. Sweeping across these are four BNS inspirals at $D = 100, 200, 400, 1000$ Mpc represented by solid (black), dotted (blue), dashed (green), and dot-dashed lines (gray), respectively. These strains sit much higher than the detector noise compared with those in Fig. 3 which foretells us that the SNRs accumulated in the ET band will be much higher, thus yielding much longer advance warning times as we show in Table IV.

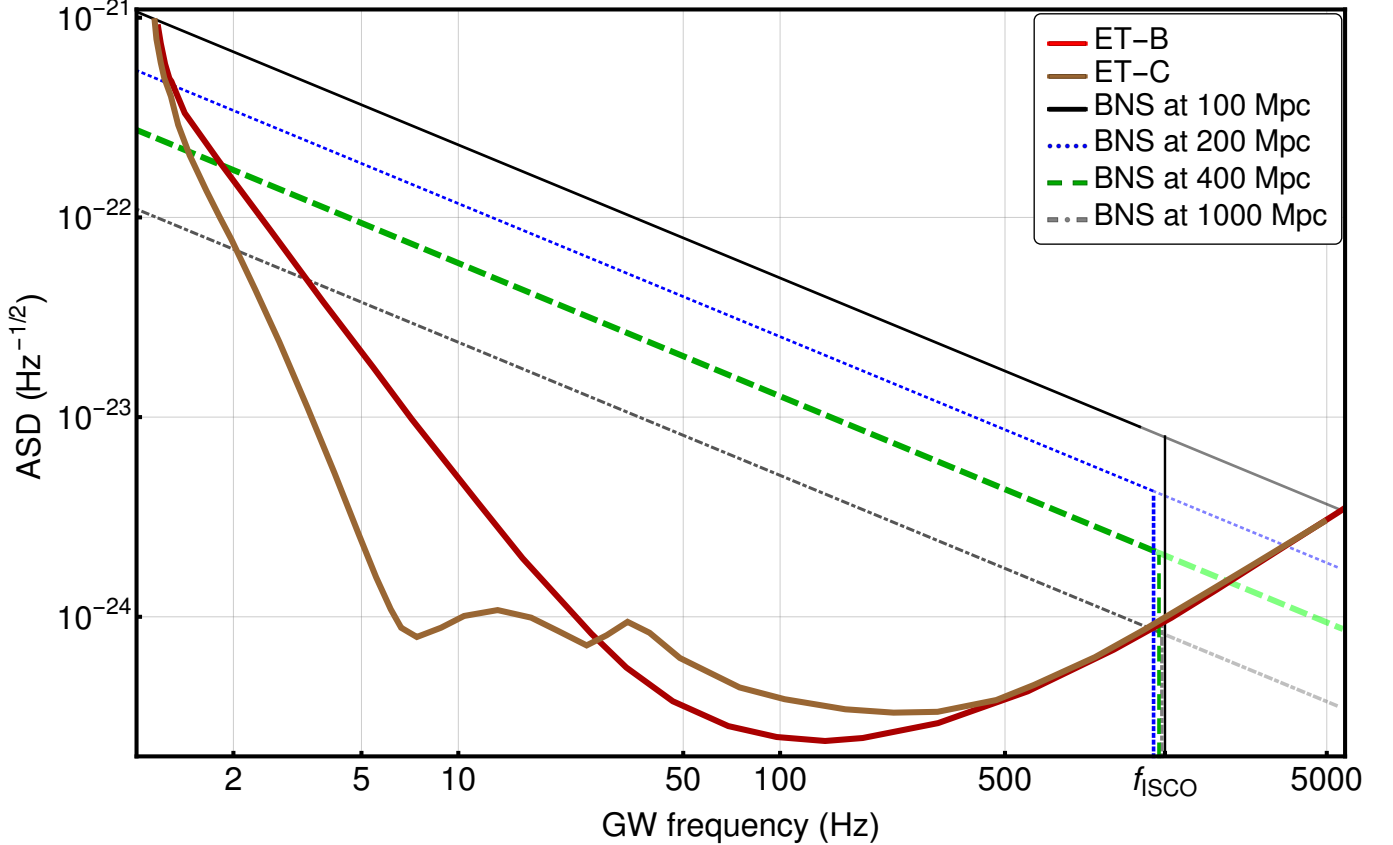


FIG. 4. Typical GW sources that may be harbingers of GRBs in the 2030s: $1.4M_\odot - 1.4M_\odot$ inspiralling BNS systems sweeping across the Einstein Telescope's sensitivity band for both B and C configurations. The solid (black), dotted (blue), dashed (green), and dot-dashed lines (gray) lines are the redshift-corrected RMS-averaged strains, $2\sqrt{f}\tilde{H}_{\text{ET}}$, at luminosity distances of $D = 100, 200, 400, 1000$ Mpc, respectively. The vertical lines with correspondingly identical patterns (colors) mark the redshifted ISCO frequencies $(1+z)^{-1}f_{\text{ISCO}}$ at which point we terminate each inspiral. As the true ISCO frequency is likely larger than f_{ISCO} [41], the inspirals would continue to nearly 2 kHz indicated by the faded lines in the plot (drawn to 5 kHz for aesthetic reasons).

To determine T_{AW} we once again impose the threshold SNR of 15 which, the reader may recall, is our detection criterion for sending out warnings to electromagnetic observatories. Thus, rewriting Eq. (6.1) in the case of ET, we define \bar{f}_{ET} as the solution to

$$\bar{\rho}_{\text{ET}}(f_0, \bar{f}_{\text{ET}}) = 15, \quad (6.7)$$

which then gives us our redshift-incorporated advance warning time via $T_{\text{AW}} = \tau_{\text{insp}}(\bar{f}_{\text{ET}})$ using Eq. (4.15) which we can slightly improve by using the 3.5PN expression. Therefore, we proceed as summarized in Fig. 2 and compute the 0PN and 3.5PN

advance warning times for all four inspirals in both the ET-B and ET-C bands. The 3.5PN computation requires rescaling of the PN parameters x and Θ to $(1+z)^{2/3}x$ and $(1+z)^{-1}\Theta$ (see Sec. 9.3 of Blanchet’s review [14] for details). The final accumulated SNRs are given by

$$\bar{\rho}_F \equiv \bar{\rho}_{\text{ET}}(f_0, f_{\text{ISCO}}). \quad (6.8)$$

where f_{ISCO} is now the redshifted version of Eq. (4.1), equalling 1537, 1505, 1448, 1311 Hz, respectively for $D = 100, 200, 400, 1000$ Mpc. Table IV summarizes our results for both ET-B and ET-C where we chose to only display the 3.5PN-accurate inspiral time as T_{AW} , but we computed this quantity also using both 0PN and 2PN expressions as a consistency check.

D (Mpc)	ET-B			ET-C		
	\bar{f}_{ET} (Hz)	T_{AW}	$\bar{\rho}_F$	\bar{f}_{ET} (Hz)	T_{AW}	$\bar{\rho}_F$
100	≈ 6.72	47.0 minutes	306	≈ 3.27	5.34 hours	365
200	≈ 11.2	11.6 minutes	152	≈ 4.10	2.87 hours	182
400	≈ 18.2	3.00 minutes	75.7	≈ 5.06	1.51 hours	90.5
1000	≈ 41.3	17.2 seconds	29.8	≈ 6.76	35.6 minutes	35.6

TABLE IV. Forecasting capabilities of Einstein Telescope summarized. ET-B and ET-C refer to the different configurations shown in Fig. 4. For the advance warning times, we only present the result of the more accurate 3.5PN computation. \bar{f}_{ET} is the threshold frequency at which ET-B/C accumulate SNR of 15 which we take to be our detection criterion. Note that both T_{AW} and $\bar{\rho}_F$ are larger for ET-C due to its improved sensitivity in the $1 \text{ Hz} \lesssim f \lesssim 30 \text{ Hz}$ regime compared to ET-B as is clear in Fig. 4. These results and those of Table. III are summarized in Fig. 5.

As the results of Table IV indicate, ET-B will provide $\gtrsim 10$ minutes of warning time for BNS inspirals at $D \lesssim 200$ Mpc. Instead of speculating whether or not this is enough to forecast GRBs, we turn our attention to ET-C’s forecasting capabilities. As can be seen from Fig. 4, ET-C’s increased sensitivity in the $1 \text{ Hz} \lesssim f \lesssim 30 \text{ Hz}$ regime will significantly lengthen the advance warning times. This is best highlighted by the sixth column of Table IV, where we show that ET-C will provide up to *five hours* of early warning time for nearby ($D \lesssim 100$ Mpc) neutron star mergers. Moreover, BNS inspirals as far as 200 Mpc (the ALV network’s horizon distance) will persist in the ET-C sensitivity band for a few hours after their initial detection ($T_{\text{AW}} > 2$ hours). Current BNS merger rate, inferred from A-LIGO’s O1-O2 periods, implies that ~ 40 to ~ 600 sources within a volume of $(200 \text{ Mpc})^3$ will be detected yearly by ET.

Given Moore’s law and new search approaches (e.g., see Ref. [66] for one based on deep learning) we speculate that the advances in the detection, localization and early-warning algorithms in the next decade will reduce the required advance warning time to less than an hour; thus we set $T_{\text{AW}} = 1$ hour and obtain corresponding BNS horizon distances of $D_H = 87$ and 613 Mpc ($z \approx 0.02, 0.127$) for ET-B and ET-C, respectively. In other words, all inspiralling BNSs closer than D_H will give us more than an hour’s leeway before the GRB (employing the detection criterion $\text{SNR} = 15$ as before). The volume set by $D = D_H$ translates to a BNS merger rate of $\sim \mathcal{O}(1)$ for ET-B and $\approx 355^{+730}_{-280} \text{ year}^{-1}$ for ET-C. Additionally, each source within D_H will accumulate $\bar{\rho}_F \gtrsim 420, 58$ over its inspiral in the ET-B, ET-C bands, respectively. These results are summarized in Table V.

Both Tables IV and V clearly show that ET will yield superb SNRs for sources out to 1 Gpc. With such high SNRs we expect that a future network consisting of ET and LIGO Voyager will be able to localize half the sources at $D \approx 1000$ Mpc to within 10 deg^2 and more than half the sources at $D \lesssim 400$ Mpc to $\approx 1 \text{ deg}^2$ [67]. Therefore, we optimistically conclude that 2030s hold in store real-time observations of dozens to hundreds of gamma-ray bursts⁴. We summarize our main findings for both the ALV network and ET-B/C in Fig. 5.

VII. Binary black hole neutron star systems

In this section, we investigate the possibility of witnessing the tidal disruption of a neutron star by a black hole before the merger. The treatment of the inspiral is the same as before, however the fate of the neutron star depends strongly on the system’s intrinsic parameters such as the black hole mass and spin, and the neutron star’s equation of state (EOS) and compactness

⁴ As the ET construction/commissioning timeline is currently uncertain, we can only speculate that ET-C will be operational after 2030, which is roughly in line with the milli-Hertz space interferometer LISA’s timeline [68].

	ET-B	ET-C
D_H	87 Mpc	613 Mpc
$R(D_H)$	$1^{+2}_{-1} \text{ yr}^{-1}$	$355^{+730}_{-280} \text{ yr}^{-1}$
$\bar{\rho}_F(D_H)$	420	58

TABLE V. Horizon distances of ET-B and ET-C assuming $T_{\text{AW}} = 1$ hour. $R(D_H)$ is the BNS merger rate within a volume of D_H^3 obtained by rescaling the rate inferred from Advanced LIGO’s O1, O2 observing periods [5]. $\bar{\rho}_F(D_H)$ is the total SNR accumulated due to a BNS inspiralling at D_H [see Eq. (6.8)].

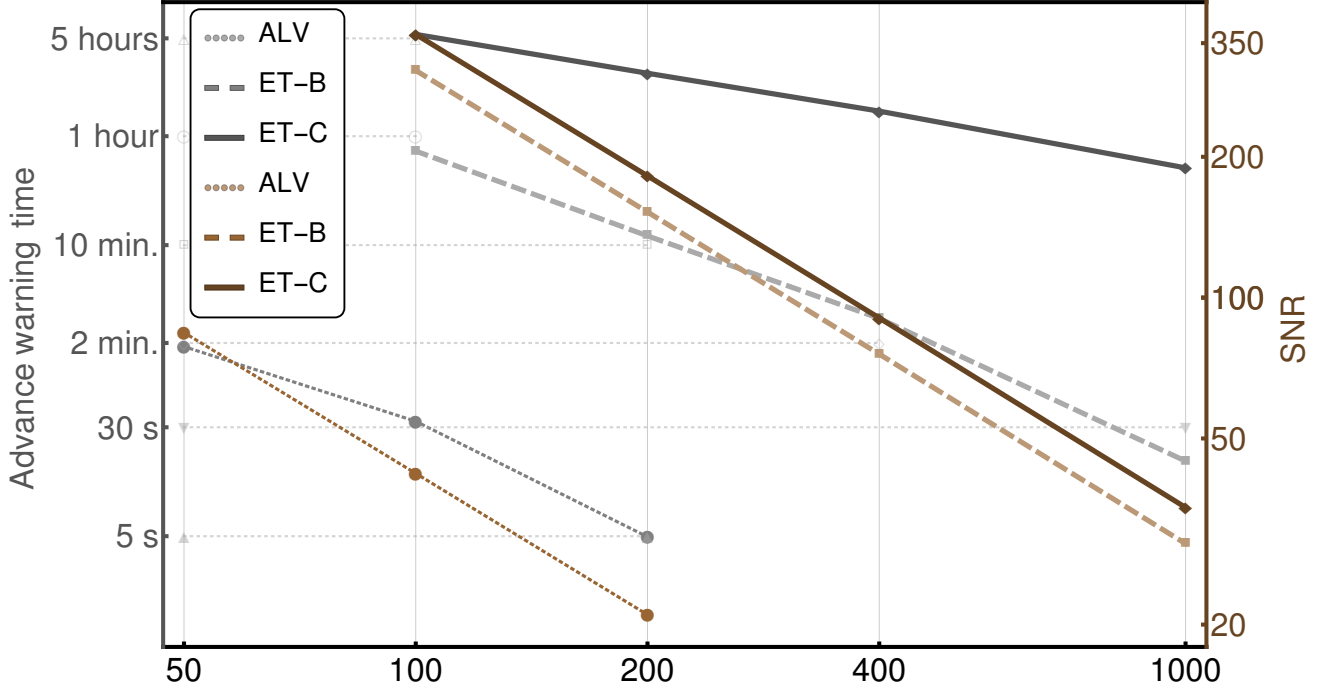


FIG. 5. Summary of our major findings for both the Advanced-LIGO-Virgo (ALV) network circa 2020 and the Einstein Telescope’s B and C configurations ca. 2030. The light coloured (gray) data shows T_{AW} for the ALV2020 (dotted), ET-B (dashed), and ET-C (solid), respectively. The connecting light (gray) lines are drawn only for visualization purposes unlike the dark (brown) lines coming from the D^{-1} powerlaw of the SNR [see Eq. (6.4)] which is plotted on the right axis. We used $D = 50, 100, 200$ Mpc to obtain the ALV results (Sec. VI 1) and $D = 100, 200, 400, 1000$ Mpc for the ET results.

$c_{\text{NS}} \equiv GM_{\text{NS}}/(R_{\text{NS}}c^2)$. The evolution of black hole-neutron star (BH-NS) binaries is a very active field of research at the interface of numerical relativity and high-energy astrophysics (see Ref. [69] for a comprehensive review) requiring fully general relativistic magnetohydrodynamic treatment including neutrino transport equations. The complexity of evolving the dynamics of these systems require large computational resources and long runtimes. As such, the details are beyond the scope of this article, but we can use a mostly Newtonian treatment to serve our purposes.

A necessary, but insufficient, condition for tidal disruption (TD) is that

$$\frac{2GM_{\text{BH}}(c_R R_{\text{NS}})}{r^3} \gtrsim \frac{GM_{\text{NS}}}{(c_R R_{\text{NS}})^2}, \quad (7.1)$$

where r is the orbital radius, R_{NS} is the radius of the NS and M denotes masses. $c_R R_{\text{NS}}$ is the semi-major axis of the elongated oblate spheroid that represents the tidally distorted shaped of the NS to leading order with $c_R > 1$. The above conditions roughly

implies

$$\frac{M_{\text{BH}}}{M_{\text{NS}}} \gtrsim \left(\frac{r}{R_{\text{NS}}} \right)^3. \quad (7.2)$$

We wish to maximize the chances of observing a TD event, therefore we ingrain the BH-NS binary with certain desirable features some of which can be deduced from Eqs. (7.1, 7.2). These are

- (i) Small separation. As the Newtonian tidal force due to the black hole is proportional to M_{BH}/r^3 , r has to be minimized to provide maximum tidal force. However, for $r < r_{\text{ISCO}}$ the NS simply plunges into the BH; therefore the minimum separation is given by the ISCO radius.
- (ii) Low black hole mass. In the test-mass case, $r_{\text{ISCO}} \propto M_{\text{BH}}$, so the Newtonian tidal force roughly scales as $M_{\text{BH}}/r_{\text{ISCO}}^3 \propto M_{\text{BH}}^{-2}$. Hence, M_{BH} must also be minimized. As is the case with r , there is also a lower bound to M_{BH} set from astrophysical observations and stellar evolution models, which currently yield $M_{\text{BH}} \gtrsim 5M_{\odot}$ [70–74].
- (iii) High black hole spins. r_{ISCO} is much smaller in the case of a prograde NS orbit around a spinning Kerr black hole. For instance, for the maximum dimensionless BH spin value of $a \equiv cJ_{\text{BH}}/(GM_{\text{BH}}^2) = 1$, r_{ISCO} for prograde orbits is 1/6th of the Schwarzschild value $6GM_{\text{BH}}/c^2$ whereas for $a = 1$ retrograde orbits, r_{ISCO} is 3/2 of the Schwarzschild value. With smaller ISCO separation, there is much more tidal force exerted on the NS before it plunges in.
- (iv) Less compact neutron stars. Eq. (7.1) can be rearranged to isolate c_{NS} on the right hand side. Smaller values for c_{NS} mean that TD is more likely to occur for $r > r_{\text{ISCO}}$.

Although the results from each numerical study of BH-NS mergers may somewhat vary what is clear is that we must have high spin and low mass for the black hole for tidal disruption to happen. We are thus led to set $M_{\text{BH}} = 5M_{\odot}$. This raises an interesting astrophysical question as to whether it is possible to have such light-weight high-spin black holes assuming that they are spun up by accretion from their secondary (that will later on become a NS) in binary systems, thus they will have to gain mass. It is possible that the mass gain pushes M_{BH} too high to either cause a direct plunge of the NS before TD or decrease τ_{insp} considerably to eliminate any chances of getting an advance warning. However, if the spin of the BH comes from the supernova explosion mechanism itself as argued for G1915 in Ref. [75] then it is possible to have a low-mass BH in a binary system⁵.

There is additional motivation to choose low BH mass as $\tau_{\text{insp}} \propto M_c^{-5/3} = (1 + Q)^{1/3}/Q$ for $Q \equiv M_{\text{BH}}/M_{\text{NS}} > 1$, which scales as $Q^{-2/3}$ as $Q \rightarrow \infty$, i.e., heavier binaries inspiral faster so it is desirable to minimize Q . Setting $M_{\text{NS}} = 1.4M_{\odot}$ as before gives $Q = 5/1.4 \simeq 3.571$. c_{NS} is determined by the radius of the NS constrained to be in the 9.9 – 11.2 km range [76] which results in $0.13 \lesssim c_{\text{NS}} \lesssim 0.15$ for our chosen NS mass. If we pick the more pessimistic $c_{\text{NS}} = 0.15$ bound then we must have $Q \lesssim 5$ and $a \gtrsim 0.5$ (prograde) for TD to occur [77] and $Q < 3$ in the case of $a = 0$ [78].

So, we simply assume that such lightweight, high-spin BHs exist in BH-NS binaries and compute strains and SNRs accordingly. A quick calculation shows that these systems yield $T_{\text{AW}} \lesssim 30$ seconds in the ALV network of 2020s. Therefore, we simply focus on the capabilities of ET which we summarize in Table VI below.

D (Mpc)	ET-B		ET-C	
	T_{AW}	$\bar{\rho}_F$	T_{AW}	$\bar{\rho}_F$
100	28.2 minutes	503	2.15 hours	601
200	8.21 minutes	251	1.10 hours	300
400	2.00 minutes	124	34.2 minutes	148
1000	14.3 seconds	49	13.9 minutes	58.5

TABLE VI. Same as Table IV, but now for a $5M_{\odot} - 1.4M_{\odot}$ black hole-neutron star binary. The SNRs are even higher than before, however the advance warning times have decreased significantly.

⁵ We thank Dr. Morgan Fraser for pointing this out.

From the table, we can see that the horizon distance of ET-C for these binaries with $T_{\text{AW}} \approx 1$ hour is roughly 200 Mpc. Given that the LIGO O1 merger rate for these systems is $R < 3600 \text{ Gpc}^{-3} \text{ yr}^{-1}$ [79], there could be ≈ 30 such mergers per year within ET-C’s horizon distance of ≈ 200 Mpc. We must emphasize that this should be viewed as an upper limit as low-mass, high-spin black holes such as ours above are expected to be rare. Theoretical studies indicate that $\lesssim 10\%$ stellar-mass BHs have masses $\lesssim 5M_{\odot}$ [80]. This seems to be supported at least by observations of galactic black holes [72]. Therefore, we realistically expect ET-C to forecast $\lesssim 3$ tidal disruption events per year.

VIII. Outlook

By constructing representative models of the near-future ground-based gravitational-wave interferometers, we investigated the possibility of forecasting gamma-ray burts resulting from the merger of two neutron stars. We showed that we do not expect the Advanced-LIGO-Virgo network to provide such a forecast in the 2020s unless we get extremely lucky and detect a binary neutron star inspiral in our galaxy, which is roughly a one-in-a-trillion shot (in years). However, the odds completely change in our favour with Einstein Telescope’s B and especially C configurations, the latter of which is expected to forecast $\gtrsim \mathcal{O}(10^2)$ gamma-ray bursts per year as we show in Table V. The same configuration should also forecast up to three tidal disruption events per year in which a high-spin, low-stellar-mass black hole tidally tears apart its companion neutron star. The beginning of operation for the C configuration will roughly coincide with the launch of the LISA mission. Additionally, there are proposals to launch another space interferometer called DECIGO which will operate in the $0.1 - 10$ Hz range thus bridging the gap between LISA and the ground-based interferometers [81, 82]. With the gravitational-wave sky virtually covered from 10^{-4} to 10^3 Hz, we will suffer from the embarrassment of the riches in the 2030s. In short, the future of gravitational and multi-messenger astronomy is bright.

Acknowledgments

SA thanks Conor O’Toole for endless feedback and Niels Warburton for a careful reading of this article.

-
- [1] B. P. Abbott *et al.* (Virgo, LIGO Scientific), *Phys. Rev.* **X6**, 041015 (2016), [arXiv:1606.04856 \[gr-qc\]](#).
 - [2] B. P. Abbott *et al.* (Virgo, LIGO Scientific), *Astrophys. J.* **851**, L35 (2017), [arXiv:1711.05578 \[astro-ph.HE\]](#).
 - [3] B. P. Abbott *et al.* (Virgo, LIGO Scientific), *Phys. Rev. Lett.* **119**, 141101 (2017), [arXiv:1709.09660 \[gr-qc\]](#).
 - [4] B. P. Abbott *et al.* (VIRGO, LIGO Scientific), *Phys. Rev. Lett.* **118**, 221101 (2017), [arXiv:1706.01812 \[gr-qc\]](#).
 - [5] B. Abbott *et al.* (Virgo, LIGO Scientific), *Phys. Rev. Lett.* **119**, 161101 (2017), [arXiv:1710.05832 \[gr-qc\]](#).
 - [6] B. P. Abbott *et al.* (Virgo, LIGO Scientific), *Phys. Rev. Lett.* **116**, 061102 (2016), [arXiv:1602.03837 \[gr-qc\]](#).
 - [7] The Fermi Collaboration, Fermi-Gamma-Ray-Burst Monitor GCN, 524666471, (2017).
 - [8] D. Svinkin *et al.*, Fermi-INTEGRAL GCN, 21515 (2017).
 - [9] V. Savchenko *et al.*, *Astrophys. J.* **848**, L15 (2017), [arXiv:1710.05449 \[astro-ph.HE\]](#).
 - [10] D. A. Coulter *et al.*, 1M2H GCN, 21529 and 21567 (2017).
 - [11] D. A. Coulter *et al.*, *Science* (2017), [10.1126/science.aap9811](#), [arXiv:1710.05452 \[astro-ph.HE\]](#).
 - [12] B. P. Abbott *et al.* (GROND, SALT Group, OzGrav, DFN, INTEGRAL, Virgo, Insight-Hxmt, MAXI Team, Fermi-LAT, J-GEM, RATIR, IceCube, CAASTRO, LWA, ePESSTO, GRAWITA, RIMAS, SKA South Africa/MeerKAT, H.E.S.S., 1M2H Team, IKI-GW Follow-up, Fermi GBM, Pi of Sky, DWF (Deeper Wider Faster Program), Dark Energy Survey, MASTER, AstroSat Cadmium Zinc Telluride Imager Team, Swift, Pierre Auger, ASKAP, VINROUGE, JAGWAR, Chandra Team at McGill University, TTU-NRAO, GROWTH, AGILE Team, MWA, ATCA, AST3, TOROS, Pan-STARRS, NuSTAR, ATLAS Telescopes, BOOTES, CaltechNRAO, LIGO Scientific, High Time Resolution Universe Survey, Nordic Optical Telescope, Las Cumbres Observatory Group, TZAC Consortium, LOFAR, IPN, DLT40, Texas Tech University, HAWC, ANTARES, KU, Dark Energy Camera GW-EM, CALET, Euro VLBI Team, ALMA), *Astrophys. J.* **848**, L12 (2017), [arXiv:1710.05833 \[astro-ph.HE\]](#).
 - [13] A. Buonanno, B. Iyer, E. Ochsner, Y. Pan, and B. S. Sathyaprakash, *Phys. Rev.* **D80**, 084043 (2009), [arXiv:0907.0700 \[gr-qc\]](#).
 - [14] L. Blanchet, *Living Rev. Rel.* **17**, 2 (2014), [arXiv:1310.1528 \[gr-qc\]](#).
 - [15] D. Eichler, M. Livio, T. Piran, and D. N. Schramm, *Nature* **340**, 126 (1989).
 - [16] “KAGRA website,” <http://gwcenter.icrr.u-tokyo.ac.jp/en/>.
 - [17] T. Akutsu *et al.* (KAGRA), (2017), [arXiv:1712.00148 \[gr-qc\]](#).
 - [18] T. Akutsu *et al.* (KAGRA), in *15th International Conference on Topics in Astroparticle and Underground Physics (TAUP 2017) Sudbury, Ontario, Canada, July 24-28, 2017* (2017) [arXiv:1710.04823 \[gr-qc\]](#).

- [19] B. P. Abbott *et al.* (VIRGO, LIGO Scientific), (2013), 10.1007/lrr-2016-1, [Living Rev. Rel.19,1(2016)], [arXiv:1304.0670 \[gr-qc\]](#).
- [20] M. A. et al., *Einstein gravitational wave Telescope Conceptual Design Study*, Tech. Rep. (European Commission, 2011).
- [21] “What Comes Next for LIGO? 2016 LIGO-DAWN Workshop II,” <https://wiki.ligo.org/pub/LSC/LIGOWorkshop2016/WebHome/Dawn-II-Report-SecondDraft-v2.pdf> ().
- [22] B. P. Abbott *et al.* (LIGO Scientific), *Class. Quant. Grav.* **34**, 044001 (2017), [arXiv:1607.08697 \[astro-ph.IM\]](#).
- [23] P. Kumar and B. Zhang, *Phys. Rept.* **561**, 1 (2014), [arXiv:1410.0679 \[astro-ph.HE\]](#).
- [24] B. Patricelli, M. Razzano, G. Cella, F. Fidecaro, E. Pian, M. Branchesi, and A. Stamerra, *JCAP* **1611**, 056 (2016), [arXiv:1606.06124 \[astro-ph.HE\]](#).
- [25] N. Bucciantini, B. D. Metzger, T. A. Thompson, and E. Quataert, *Mon. Not. Roy. Astron. Soc.* **419**, 1537 (2012), [arXiv:1106.4668 \[astro-ph.HE\]](#).
- [26] B. P. Abbott *et al.* (VIRGO, LIGO Scientific), *Astron. Astrophys.* **539**, A124 (2012), [arXiv:1109.3498 \[astro-ph.IM\]](#).
- [27] K. Cannon *et al.*, *Astrophys. J.* **748**, 136 (2012), [arXiv:1107.2665 \[astro-ph.IM\]](#).
- [28] T. D. Knowles, C. Devine, D. A. Buch, S. A. Bilgili, T. R. Adams, Z. B. Etienne, and S. T. McWilliams, (2018), [arXiv:1803.06346 \[gr-qc\]](#).
- [29] S. Nissanke, M. Kasliwal, and A. Georgieva, *Astrophys. J.* **767**, 124 (2013), [arXiv:1210.6362 \[astro-ph.HE\]](#).
- [30] J. A. Faber and F. A. Rasio, *Living Rev. Rel.* **15**, 8 (2012), [arXiv:1204.3858 \[gr-qc\]](#).
- [31] K. Kyutoku, K. Kiuchi, Y. Sekiguchi, M. Shibata, and K. Taniguchi, *Phys. Rev.* **D97**, 023009 (2018), [arXiv:1710.00827 \[astro-ph.HE\]](#).
- [32] F. Zappa, S. Bernuzzi, D. Radice, A. Perego, and T. Dietrich, *Phys. Rev. Lett.* **120**, 111101 (2018), [arXiv:1712.04267 \[gr-qc\]](#).
- [33] T. Dietrich, S. Bernuzzi, B. Bruegmann, and W. Tichy (2018) [arXiv:1803.07965 \[gr-qc\]](#).
- [34] A. Einstein, *Sitzungsberichte der Königlich Preußischen Akademie der Wissenschaften (Berlin)*, Seite 154-167. (1918).
- [35] A. A. Michelson and E. W. Morley, *Am. J. Sci.* **34**, 333 (1887).
- [36] B. S. Sathyaprakash and B. F. Schutz, *Living Rev. Rel.* **12**, 2 (2009), [arXiv:0903.0338 \[gr-qc\]](#).
- [37] M. Maggiore, *Gravitational Waves: Volume 1: Theory and Experiments*, Gravitational Waves (OUP Oxford, 2008).
- [38] B. Sathyaprakash *et al.*, *Gravitational waves. Numerical relativity - data analysis. Proceedings, 9th Edoardo Amaldi Conference, Amaldi 9, and meeting, NRDA 2011, Cardiff, UK, July 10-15, 2011*, *Class. Quant. Grav.* **29**, 124013 (2012), [Erratum: *Class. Quant. Grav.*30,079501(2013)], [arXiv:1206.0331 \[gr-qc\]](#).
- [39] L. Wen and B. F. Schutz, *Gravitational wave data analysis. Proceedings, 9th Workshop, GWDAW 2004, Annecy, France, December 15-18, 2004*, *Class. Quant. Grav.* **22**, S1321 (2005), [arXiv:gr-qc/0508042 \[gr-qc\]](#).
- [40] T. Regimbau *et al.*, *Phys. Rev.* **D86**, 122001 (2012), [arXiv:1201.3563 \[gr-qc\]](#).
- [41] P. Marronetti, M. D. Duez, S. L. Shapiro, and T. W. Baumgarte, *Phys. Rev. Lett.* **92**, 141101 (2004), [arXiv:gr-qc/0312036 \[gr-qc\]](#).
- [42] F. Özel and P. Freire, *Ann. Rev. Astron. Astrophys.* **54**, 401 (2016), [arXiv:1603.02698 \[astro-ph.HE\]](#).
- [43] P. C. C. Freire, S. M. Ransom, S. Begin, I. H. Stairs, J. W. T. Hessels, L. H. Frey, and F. Camilo, *Astrophys. J.* **675**, 670 (2008), [arXiv:0711.0925 \[astro-ph\]](#).
- [44] P. C. Peters and J. Mathews, *Phys. Rev.* **131**, 435 (1963).
- [45] R. A. Hulse and J. H. Taylor, *Astrophys. J.* **195**, L51 (1975).
- [46] J. M. Weisberg, D. J. Nice, and J. H. Taylor, *Astrophys. J.* **722**, 1030 (2010), [arXiv:1011.0718 \[astro-ph.GA\]](#).
- [47] M. Colpi and A. Sesana, in *An Overview of Gravitational Waves: Theory, Sources and Detection*, edited by G. Auger and E. Plagnol (2017) pp. 43–140, [arXiv:1610.05309 \[astro-ph.HE\]](#).
- [48] J. W. T. Hessels, S. M. Ransom, I. H. Stairs, P. C. C. Freire, V. M. Kaspi, and F. Camilo, *Science* **311**, 1901 (2006), [arXiv:astro-ph/0601337 \[astro-ph\]](#).
- [49] E. S. Phinney, (2001), [arXiv:astro-ph/0108028 \[astro-ph\]](#).
- [50] “GW170817 Factsheet,” https://www.ligo.org/detections/GW170817/images-GW170817/GW170817_Factsheet.pdf.
- [51] L. Bernard, L. Blanchet, G. Faye, and T. Marchand, (2017), [arXiv:1711.00283 \[gr-qc\]](#).
- [52] “Data release for GW170817,” <https://losc.ligo.org/events/GW170817/> ().
- [53] “LIGO Open Science Center signal processing tutorial,” https://losc.ligo.org/s/events/GW150914/GW150914_tutorial.html ().
- [54] J. S. Read, C. Markakis, M. Shibata, K. Uryu, J. D. E. Creighton, and J. L. Friedman, *Phys. Rev.* **D79**, 124033 (2009), [arXiv:0901.3258 \[gr-qc\]](#).
- [55] “Advanced LIGO anticipated sensitivity curves,” <https://dcc.ligo.org/LIGO-T0900288/public> ().
- [56] C. Cutler and E. E. Flanagan, *Phys. Rev.* **D49**, 2658 (1994), [arXiv:gr-qc/9402014 \[gr-qc\]](#).
- [57] B. Farr *et al.*, *Astrophys. J.* **825**, 116 (2016), [arXiv:1508.05336 \[astro-ph.HE\]](#).

- [58] C. L. Rodriguez, B. Farr, V. Raymond, W. M. Farr, T. B. Littenberg, D. Fazi, and V. Kalogera, *Astrophys. J.* **784**, 119 (2014), [arXiv:1309.3273 \[astro-ph.HE\]](#).
- [59] X. Zhu, E. Thrane, S. Oss, Y. Levin, and P. D. Lasky, (2017), [arXiv:1711.09226 \[astro-ph.HE\]](#).
- [60] N. Andersson, V. Ferrari, D. I. Jones, K. D. Kokkotas, B. Krishnan, J. S. Read, L. Rezzolla, and B. Zink, *Gen. Rel. Grav.* **43**, 409 (2011), [arXiv:0912.0384 \[astro-ph.SR\]](#).
- [61] L. Wade, J. D. E. Creighton, E. Ochsner, B. D. Lackey, B. F. Farr, T. B. Littenberg, and V. Raymond, *Phys. Rev. D* **89**, 103012 (2014).
- [62] B. D. Lackey and L. Wade, *Phys. Rev. D* **91**, 043002 (2015).
- [63] R. Adam *et al.* (Planck), *Astron. Astrophys.* **594**, A1 (2016), [arXiv:1502.01582 \[astro-ph.CO\]](#).
- [64] D. W. Hogg, (1999), [arXiv:astro-ph/9905116 \[astro-ph\]](#).
- [65] S. Hild *et al.*, *Class. Quant. Grav.* **28**, 094013 (2011), [arXiv:1012.0908 \[gr-qc\]](#).
- [66] H. Gabbard, M. Williams, F. Hayes, and C. Messenger, (2017), [arXiv:1712.06041 \[astro-ph.IM\]](#).
- [67] J. Mills, V. Tiwari, and S. Fairhurst, (2017), [arXiv:1708.00806 \[gr-qc\]](#).
- [68] P. Amaro-Seoane *et al.*, (2017), [arXiv:1702.00786 \[astro-ph.IM\]](#).
- [69] M. Shibata and K. Taniguchi, *Living Rev. Rel.* **14**, 6 (2011).
- [70] W. M. Farr, N. Sravan, A. Cantrell, L. Kreidberg, C. D. Bailyn, I. Mandel, and V. Kalogera, *Astrophys. J.* **741**, 103 (2011), [arXiv:1011.1459 \[astro-ph.GA\]](#).
- [71] C. A. Raithel, T. Sukhbold, and F. Özel, (2017), [arXiv:1712.00021 \[astro-ph.HE\]](#).
- [72] F. Özel, D. Psaltis, R. Narayan, and J. E. McClintock, *Astrophys. J.* **725**, 1918 (2010), [arXiv:1006.2834 \[astro-ph.GA\]](#).
- [73] G. Wiktorowicz, K. Belczynski, and T. J. Maccarone, (2013), [arXiv:1312.5924 \[astro-ph.HE\]](#).
- [74] P. Christian, P. Mocz, and A. Loeb, (2018), [arXiv:1803.07094 \[astro-ph.HE\]](#).
- [75] J. E. McClintock, R. Shafee, R. Narayan, R. A. Remillard, S. W. Davis, and L.-X. Li, *Astrophys. J.* **652**, 518 (2006), [arXiv:astro-ph/0606076 \[astro-ph\]](#).
- [76] F. Özel and P. Freire, *Ann. Rev. Astron. Astrophys.* **54**, 401 (2016), [arXiv:1603.02698 \[astro-ph.HE\]](#).
- [77] V. Ferrari, L. Gualtieri, and F. Pannarale, *Class. Quant. Grav.* **26**, 125004 (2009), [arXiv:0801.2911 \[astro-ph\]](#).
- [78] K. Kyutoku, H. Okawa, M. Shibata, and K. Taniguchi, *Phys. Rev. D* **84**, 064018 (2011), [arXiv:1108.1189 \[astro-ph.HE\]](#).
- [79] B. P. Abbott *et al.* (Virgo, LIGO Scientific), *Astrophys. J.* **832**, L21 (2016), [arXiv:1607.07456 \[astro-ph.HE\]](#).
- [80] C. L. Fryer and V. Kalogera, *Astrophys. J.* **554**, 548 (2001), [arXiv:astro-ph/9911312 \[astro-ph\]](#).
- [81] S. Sato *et al.*, *Laser Interferometer Space Antenna. Proceedings, 7th international LISA Symposium, Barcelona, Spain, June 16-20, 2008*, *J. Phys. Conf. Ser.* **154**, 012040 (2009).
- [82] S. Kawamura *et al.*, in *Recent developments in theoretical and experimental general relativity, gravitation and relativistic field theories. Proceedings, 11th Marcel Grossmann Meeting, MG11, Berlin, Germany, July 23-29, 2006. Pt. A-C* (2006) pp. 2393–2397.